The ALMA REBELS Survey: dust continuum detections at $z > 6.5$

Hanae Inami [1]★ Hiddo S. B. Algera,[1,2] Sander Schouws,[3] Laura Sommovigo,[4] Rychard Bouwens,[3]★
Renske Smit,[5] Mauro Stefanon [3] Rebecca A. A. Bowler [6] Ryan Endsley [7] Andrea Ferrara,[4]
Pascal Oesch,[8,9] Daniel Stark,[7] Manuel Aravena,[10] Laia Barrufet,[8] Elisabete da Cunha,[11]
Pratika Dayal [12] Ilse De Looze [13,14] Yoshinobu Fudamoto,[2,15] Valentino Gonzalez,[16,17]
Luca Graziani [18,19] Jacqueline A. Hodge,[3] Alexander P. S. Hygate [3] Themiya Nanayakkara [20]
Andrea Pallottini [4] Dominik A. Riechers,[21] Raffaella Schneider [18,22] Michael Topping[7]
and Paul van der Werf[3]

Affiliations are listed at the end of the paper

ABSTRACT

We report 18 dust continuum detections ($\geq 3.3\sigma$) at $\sim$88 and 158 μm out of 49 ultraviolet (UV)-bright galaxies ($M_{UV} < -21.3$ mag) at $z > 6.5$, observed by the Cycle-7 Atacama Large Millimeter/submillimeter Array (ALMA) Large Program, Reionization-Era Bright Emission Line Survey (REBELS) and its pilot programs. This has more than tripled the number of dust continuum detections known at $z > 6.5$. Out of these 18 detections, 12 are reported for the first time as part of REBELS. In addition, 15 of the dust continuum detected galaxies also show a [C II]$_{158 \mu m}$ emission line, providing us with accurate redshifts. We anticipate more line emission detections from six targets (including three continuum detected targets) where observations are still ongoing. We estimate that all of the sources have an infrared (IR) luminosity (L_{IR}) in a range of $3–8 \times 10^{11}$ L$_\odot$, except for one with $L_{IR} = 1.5^{+0.8}_{-0.5} \times 10^{12}$ L$_\odot$. Their fraction of obscured star formation is significant at $\gtrsim 50$ per cent, despite being UV-selected galaxies. Some of the dust continuum detected galaxies show spatial offsets ($\sim$0.5–1.5 arcsec) between the rest-UV and far-IR emission peaks. These separations could imply spatially decoupled phases of obscured and unobscured star formation, but a higher spatial resolution observation is required to confirm this. REBELS offers the best available statistical constraints on obscured star formation in UV-luminous galaxies at $z > 6.5$.

Key words: methods: observational – galaxies: evolution – galaxies: formation – galaxies: high-redshift – galaxies: ISM – infrared: galaxies.

1 INTRODUCTION

While cosmic dust constitutes only a small fraction (<1 per cent) of the total mass of the interstellar medium (ISM), it plays a major role in characterizing galaxy properties and in influencing galaxy evolution (Sparke & Gallagher 2000). Dust absorbs and scatters ultraviolet (UV) and optical emission, and reradiates the absorbed energy in the infrared (IR) as thermal emission. Thus, far-IR emission from dust traces obscured star formation, which is key to obtaining a complete census of star formation in the Universe. The IR star formation rate density increases with redshift at least up to $z \sim 2–3$ and dominates the total star formation rate density in this redshift range (e.g. Gruppioni et al. 2013; Magnelli et al. 2013; Madau & Dickinson 2014; Novak et al. 2017).

With the advent of the Atacama Large Millimeter/submillimeter Array (ALMA), detections of dusty star-forming galaxies at higher redshift ($z \gtrsim 3$) have been steadily increasing, enabling some more complete studies of dust-embedded star formation in the distant universe (for a review see Hodge & da Cunha 2020). In particular,

large surveys have been pushing forwards our understanding of obscured star formation at high redshifts. Multiple deep surveys in the Great Observatories Origins Deep Survey-South (GOODS-South) field have characterized the detailed properties of galaxies, mostly at $z = 2–4$, that contribute to obscured star formation (Dunlop et al. 2017; Yamaguchi et al. 2019, 2020; Aravena et al. 2020; Franco et al. 2020a,b; González-López et al. 2020).

A prediction of obscured star formation out to $z = 7$ has been made by Zavala et al. (2021) (see also Casey et al. 2021), combining a shallower but wide area 2-mm survey with the ultradeep 1- and 3-mm surveys (González-López et al. 2019, 2020). The ALMA Large Program to INvestigate [C II] at Early times (ALPINE) has revealed dusty star formation at $z \sim 5.5$ with their main target galaxies (Khusanova et al. 2021) and at $1 \lesssim z \lesssim 6$ with serendipitously detected galaxies in the fields that they targeted (Gruppioni et al. 2020). The current census seems to indicate that the obscured star formation density starts to decrease from $z \sim 2–3$ towards higher redshift, but how fast it declines is still uncertain.

In addition, direct comparisons between the far-IR and UV emission have revealed that there is potentially an evolution in the relationship between the infrared excess (IRX = L_{IR}/L_{UV}) and the UV spectral slope (β_{UV}) or stellar mass (M_*; Capak et al. 2015;

Bouwens et al. 2016, 2020; Barisic et al. 2017; Koprowski et al. 2018; McLure et al. 2018; Fudamoto et al. 2020; Bowler et al. 2022). Beside uncertainties on L_{IR} often being large at high redshift, this could imply that a different attenuation curve may need to be adopted when UV and dust emission coexist. However, there are some cases that show spatial offsets between UV and dust emission, making it harder to interpret the difference seen in IRX–β_{UV} (or M_*) in the distant (and local) universe (e.g. Howell et al. 2010; Hodge et al. 2012, 2016; Koprowski et al. 2016; Carniani et al. 2017; Laporte et al. 2017; Popping, Puglisi & Norman 2017). Furthermore, if a spatial offset between UV and far-IR is common among high-redshift galaxies (e.g. Behrens et al. 2018; Liang et al. 2019; Ma et al. 2019; Sommovigo et al. 2020), stacking of far-IR data based on UV locations will not present the full picture of the dust emission.

Dust is not only responsible for obscured star formation, but also regulates the evolution of galaxies by, for example, contributing to heating of the gas in the ISM by photoelectric heating (e.g. Nath, Sethi & Shchekinov 1999) and facilitating molecular gas (H_2) formation on its grain surfaces (e.g. Wakelam et al. 2017). However, the first emergence of dust and its build-up at the beginning of the Universe is still unknown. Attempts at searching for dusty galaxies in the distant universe have been extended to the epoch of reionization. Recent ALMA observations, despite the small number of detections, enable us to discern mounting evidence that significant obscured star formation was already taking place in some normal galaxies as early as ∼600 Myr after the big bang (Watson et al. 2015; Knudsen et al. 2017; Laporte et al. 2017, 2021; Bowler et al. 2018, 2022; Hashimoto et al. 2019; Tamura et al. 2019; Bakx et al. 2020, 2021; Fudamoto et al. 2021; Sugahara et al. 2021; Schouws et al. 2022a). A large number of theoretical studies have also been conducted to try to guide interpretations of these observed galaxies (e.g. Aoyama et al. 2017, 2018; Behrens et al. 2018; Ginolfi et al. 2018; Graziani et al. 2020; Pallottini et al. 2022).

A mechanism of fast dust formation or grain growth may be required at such an early era of the Universe (≲1 Gyr) to produce the observed dust mass (Mancini et al. 2015, 2016; Ginolfi et al. 2018; Graziani et al. 2020). On the other hand, there are other models coupling the baryonic and dust assembly of early galaxies, which show that even invoking ISM dust growth time-scales as short as 0.3 Myr can only scale up the dust mass by a factor of 2 (Dayal et al. 2022). For low-mass stars ($< 8\,M_\odot$), their lifetime is too long to evolve into the asymptotic giant branch (AGB) phase by $z \sim 7$. Thus, supernovae are likely the major stellar source contributor producing the dust in galaxies at $z \gtrsim 7$ (Mancini et al. 2015; Leśniewska & Michałowski 2019; Sommovigo et al. 2020; Dayal et al. 2022). With existing observations, we have increasingly gained some perspective on the dust properties of some galaxies at high redshifts, but the limited number of detections has made it difficult to characterize the properties in a statistical way.

The ALMA Cycle-7 Large Program, Reionization-Era Bright Emission Line Survey (REBELS; Bouwens et al. 2022), aims to obtain a statistical sample of luminous star-forming galaxies at $z > 6.5$. REBELS is designed to acquire spectroscopic redshifts from an ISM cooling line and simultaneously detect dust continuum emission. This ongoing large survey targets 40 UV-luminous Lyman-break galaxies selected over ∼7 deg² to search for the [C II]$_{158\,\mu m}$ or [O III]$_{88\,\mu m}$ emission lines with spectral scans. As shown in Bouwens et al. (2022) and the reports from the pilot programs (Smit et al. 2018; Schouws et al. 2022a,b), the observational strategy has proven to dramatically increase the number of spectroscopically confirmed galaxies and dust continuum detections at $z > 6.5$. A larger sample allows us to explore the prevalence of dust-rich galaxies, characterize

their dust properties, and study dust build-up in the early epoch of the Universe (e.g. Dayal et al. 2022; Ferrara et al. 2022; Sommovigo et al. 2022; Schneider et al., in preparation; Graziani et al., in preparation). The REBELS survey has also proved its power by making serendipitous detections at $z \sim 7$ of two heavily obscured star-forming galaxies without an optical counterpart (Fudamoto et al. 2021). The detections of [C II] emission in REBELS are reported by Schouws et al. (in preparation).

In this paper, we present dust continuum detections and flux extractions of the UV-selected luminous galaxies at $z > 6.5$ from the REBELS and pilot programs. Together with the dust properties, we also show galaxy global properties derived from the UV emission (Stefanon et al., in preparation) of the dust continuum detected galaxies. In addition, we compare the dust morphologies of these galaxies to their UV morphologies.

This paper is organized as follows. In Section 2, we describe the REBELS observations and the data reduction, followed by presenting the ancillary data used in this work. Then in Section 3, we present the method to identify dust continuum emission, measure the dust continuum flux, and calculate the total IR luminosity. Galaxy properties of the dust continuum detected sources are shown in Section 4. We discuss dust morphologies and spatial offsets between the rest-UV and IR emission in Section 5. Lastly, we summarize our findings in Section 6.

We adopt a flat Λ cold dark matter (ΛCDM) cosmology with $H = 70\,\mathrm{km\,s^{-1}\,Mpc^{-1}}$, $\Omega_M = 0.3$, and $\Omega_\Lambda = 0.7$. All magnitudes are expressed in the AB system (Oke & Gunn 1983). For star formation rates (SFRs) and stellar masses (M_*), we adopt a Chabrier initial mass function (IMF; Chabrier 2003).

2 OBSERVATIONS AND DATA REDUCTION

2.1 The REBELS program

REBELS is an ALMA Large Program in Cycle-7 (2019.1.01634.L, PI: Bouwens) that systematically targets 40 UV-luminous ($M_{UV} < -21.3$ mag) star-forming galaxies in the epoch of reionization ($z > 6.5$) to perform a spectral scan for the [C II]$_{158\,\mu m}$ or [O III]$_{88\,\mu m}$ emission line. The galaxies targeted by the REBELS survey were searched for in a total area of ∼7 deg², including Cosmological Evolution Survey (COSMOS)/UltraVISTA (Scoville et al. 2007; McCracken et al. 2012), UKIRT Infrared Deep Sky Survey (UKIDSS)/UltraDeep Survey (UDS) and VISTA Deep Extragalactic Observations (VIDEO)/*X-ray Multi-Mirror Mission* (*XMM*)-Large-Scale Structure (LSS; Lawrence et al. 2007; Jarvis et al. 2013), Cosmic Assembly Near-infrared Deep Extragalactic Legacy Survey (CANDELS; Grogin et al. 2011), Cluster Lensing And Supernova survey with *Hubble* (CLASH; Postman et al. 2012), and Brightest of Reionizing Galaxies (BoRG)/*Hubble* Infrared Pure Parallel Imaging Extragalactic Survey (HIPPIES; Trenti et al. 2011; Yan et al. 2011). In these search fields, our targets were selected to have a UV SFR of $> 10\,M_\odot\,\mathrm{yr^{-1}}$, a strong Lyman break, and a photometric redshift of $6.5 \lesssim z_{phot} \lesssim 9.5$.

The survey design is detailed in Bouwens et al. (2022) and here we provide a brief summary. To maximize the spectral scan efficiency, for the targets with $z_{phot} < 8.5$, we have observed the [C II] line with Band 5 or 6. For the targets at higher redshift, the [O III] line has been observed with Band 7. Dust continuum emission is simultaneously observed during the spectral scans of the [C II] or [O III] emission line. The observations were carried out with the most compact array configuration (C43-1 and C43-2) with a synthesized beam of ∼1.2–1.6 arcsec full width at half-maximum (FWHM).

Most of the observations were performed between 2019 November and 2020 January. There are still six targets whose observations are to be completed (REBELS-04, REBELS-06, REBELS-11, REBELS-16, REBELS-24, and REBELS-37). The completed observations constitute 87 per cent (60.6 h) of the approved total observing time of 70 h. In addition, we include the results from our pilot observations in this paper. In our first pilot study we detected [C II] in two galaxies at $z \sim 6.8$ (Smit et al. 2018) and in our second pilot study we detected dust continuum in six $z \sim 7$–8 galaxies (Schouws et al. 2022a) and [C II] in three $z \sim 7$ galaxies (Schouws et al. 2022b) (see also Table 1). For six of the galaxies from the pilot observations in which the [C II] line was not detected, they have been targeted in the main REBELS survey to scan the remainder of the redshift probability distribution. The observational set-ups for the pilot and REBELS observations are the same. We therefore include the visibility measurement sets from the pilot observations for those six sources when creating the dust continuum maps to maximize sensitivity. In total, we have targeted 49 UV-selected galaxies in the REBELS main and pilot surveys at $z > 6.5$.

2.2 ALMA data reduction and dust continuum images

The data reduction and calibration were carried out with the observatory-provided standard pipeline using the Common Astronomy Software Application (CASA) package (version 5.6.1; McMullin et al. 2007). The data cubes were then imaged using the TCLEAN task with automasking to clean down to 2σ with a cell pixel size of 0.15 arcsec and natural weighting. The dust continuum maps were created using the calibrated data cubes by excluding the frequency range that covers $2 \times$ FWHM around a detected emission line, [C II] or [O III], of the targeted source in the phase centre. A more detailed description, in particular for the procedures related to identifying an emission line in the data, can be found in Schouws et al. (in preparation).

2.3 SED fittings of UV–NIR photometries

In this work, we use the optical and near-IR (NIR) images taken by the surveys listed in Section 2.1. Based on these data, we investigate rest-frame UV properties of the dust continuum detected sources in our sample. The physical properties of the REBELS galaxies were derived from rest-UV photometries and spectral energy distribution (SED) fittings using the BEAGLE code (Chevallard & Charlot 2016). In this paper, we did not include any dust continuum measurements (or upper limits) in the BEAGLE SED fits. Here we briefly summarize the procedure. For the full description of the SED fitting and the available optical and NIR data, we refer to Stefanon et al. (in preparation).

BEAGLE utilizes the synthetic models of stellar and nebular emission from Gutkin, Charlot & Bruzual (2016) that combine the latest stellar population synthesis models of Bruzual & Charlot (2003) with the photoionization models from CLOUDY (Ferland et al. 2013). We assumed a constant star formation history (SFH),[1] a subsolar metallicity (0.2 $Z_\odot$; motivated by Stark et al. 2017; De Barros et al. 2019), and a Chabrier (2003) IMF mass cut-off of 0.1–300 $M_\odot$ to reduce a bias towards extremely young stellar population ages. We adopted the Calzetti et al. (2000) dust extinction curve. Based

on these assumptions, we derived UV magnitude (M_{UV}), β_{UV}, dust extinction in the V band (A_V), stellar age, and the equivalent width of the sum of the [O III] and Hβ emission lines via SED fitting.

2.4 Astrometry correction of the NIR images

We also explore spatial offsets between rest-UV (NIR in the observed frame) and dust emission. For all of the REBELS sample, there are J-, H-, and K-band images available, except for the two galaxies selected from the data taken with the *Hubble Space Telescope* (*HST*), REBELS-16 (MACS0429-Z1) and REBELS-40 (Super8-1), which do not have a K-band image.

The spatial offset analysis requires that all astrometry is well aligned. Based on the beam size at $\sim$1 mm, we find that the expected astrometric uncertainty of the ALMA observations is $\sim$0.2 and $\sim$0.5 arcsec at the signal-to-noise ratios (SNRs) of 5 and 3, respectively, for our continuum detections. We did not find any counterparts for either the main REBELS targets or serendipitous sources in the pointing fields with solid detections or any matching point sources in public catalogues of the Very Large Array (VLA; e.g. Smolčić et al. 2017) to perform a further examination for the astrometric alignment.

For the rest-UV data taken in the NIR bands, we either used the public images that were already aligned to a *Gaia* catalogue (UltraVISTA) or applied the astrometric correction using the *Gaia* Data Release 3 catalogue for the *XMM* and the *HST* fields (Gaia Collaboration et al. 2016, 2021) with the procedure as follows. For the REBELS sources in the *XMM* fields (*XMM* 1, *XMM* 2, or *XMM* 3, which consists of three separate tiles according to the VISTA VIRCAM footprint), the correction was not applied to an entire mosaic image but rather to a 6×6 arcmin^2 cropped image with a REBELS source at the centre to improve the local astrometry. An exception is REBELS-08; because it lies near the edge of the original *JHK* images, we shifted the centre of the cropped image by -1.8 arcmin. For the two sources (REBELS-16 and REBELS-40) observed with the *HST*, we use the full Wide Field Camera 3 (WFC3) image to maximize the number of *Gaia* sources available for registration.

We then cross-matched the *Gaia* sources in the NIR images to calculate their offsets in the XY directions. The centres of the matched sources in the NIR images were found by Gaussian fitting. The *Gaia* sources with a large parallax angle (>10 mas) were not used for the astrometric alignment. Proper motion was corrected using the *Gaia* reference epoch and the date when a NIR image was taken. When the NIR data were taken over a certain period of time (e.g. mosaic), the mid-point of the first and last date was used. The correction factor was calculated using the 3σ-clipped mean separation between the *Gaia* sources and the same sources found in the NIR image. Although each NIR-band image has its own correction factor, we used their mean value to correct for all NIR images taken within each observing program. The difference between the individual offsets and the mean offsets are small (typically a few milliarcseconds). This correction improved the astrometry to an rms of $\approx$30–120 mas between the *Gaia* stars and the corresponding sources in the NIR image.

3 EXTRACTION OF DUST CONTINUUM EMISSION

3.1 Identifying dust emission

We used PYBDSF (Mohan & Rafferty 2015) to detect dust emission in each ALMA dust continuum image without any primary beam

---

[1] In the paper, we adopt the constant SFH to facilitate comparisons to earlier studies. Note that non-parametric treatments of SFH for galaxies during the epoch of reionization could lead to a higher stellar mass. We refer to Topping et al. (2022) for the adoption of non-parametric SFHs of the REBELS galaxies and comparisons to the constant SFH values.

Table 1. Summary of the dust continuum flux measurements of the REBELS targets (the first 40 sources) and the pilot targets (the last nine sources). For the sources with a detection, we quote their Gaussian fit (CASA/IMFIT) results, while for a non-detection, the peak emission upper limit (3σ) is shown. The reported flux for REBELS-25 is the integrated flux, but the peak fluxes for the rest of the sources (Section 3.2). The rest-frame 158 μm continuum flux density is not corrected for the cosmic microwave background (CMB) effect, while the correction has been applied to L_{IR}. The redshifts are spectroscopic redshifts for the sources with a [C II] detection, otherwise they are photometric redshifts indicated by a dagger. The flux density from literature (uncorrected for the CMB effect) is taken from Schouws et al. (2022b), Smit et al. (2018), and Bowler et al. (2022), indicated as S22, S18, and B21, respectively. The two sources with the asterisk from the pilot program, UVISTA-Y-008 and UVISTA-Y-010, are listed as UVISTA-Y-007 and UVISTA-Y-009, respectively, in Schouws et al. (2022b). The ALMA source names shown in parentheses are the ones used in the ALMA Science Archive. A machine readable table is available at http://xxx on CDS.

REBELS ID	ALMA source name	Redshift	Observed frequency (GHz)	Continuum flux (μJy)	SNR	L_{IR} (10^{11} L$_\odot$)	F_ν from literature (μJy)	Literature
REBELS-01	XMM1-Z-276466	7.1771	228.12	<50	...	<2.9	...	...
REBELS-02	XMM1-35779	6.64†	248.69	<49	...	<2.5	...	...
REBELS-03	XMM1-Z-1664	6.9695	238.57	<51	...	<2.8	...	...
REBELS-04	XMM-J-355	8.57†	347.77	68 ± 20	3.4	$4.5^{+1.6}_{-2.7}$	...	...
REBELS-05	XMM1-1591	6.4963	248.69	67 ± 13	5.3	$3.2^{+1.9}_{-1.2}$	...	...
REBELS-06	XMM1-Z-151269	6.80†	244.00	77 ± 15	5.0	$4.0^{+2.3}_{-1.5}$	...	...
REBELS-07	XMM1-Z-1510	7.15†	230.97	<49	...	<2.8	...	...
REBELS-08	XMM1-67420	6.7495	246.24	101 ± 20	5.1	$5.2^{+3.0}_{-2.0}$	...	...
REBELS-09	XMM2-Z-1116453	7.61†	223.26	<53	...	<3.4	...	...
REBELS-10	XMM2-Z-564239	7.42†	223.26	<56	...	<3.4	...	...
REBELS-11	XMM3-Y-217016	8.24†	347.77	<93	...	<5.8	...	...
REBELS-12	XMM3-Z-110958	7.3459	228.12	87 ± 24	3.6	$5.2^{+3.1}_{-2.2}$	...	...
				(48 ± 13)	(3.8)	...	...	...
				(39 ± 12)	(3.3)	...	...	...
REBELS-13	XMM-J-6787	8.19†	349.67	<87	...	<5.4	...	...
REBELS-14	XMM3-Z-432815	7.0842	238.57	60 ± 15	4.1	$3.3^{+2.0}_{-1.4}$	...	...
REBELS-15	XMM3-Z-1122596	6.8752	244.00	<68	...	<3.6	...	...
REBELS-16	MACS0429-Z1	6.70†	245.90	<71	...	<3.6	...	...
REBELS-17	UVISTA-Z-1373	6.5376	248.12	<80	...	<3.9	...	...
REBELS-18	UVISTA-Y-001	7.6750	204.72	53 ± 10	5.3	$3.5^{+2.0}_{-1.3}$	73.0 ± 20.0	S22
REBELS-19	UVISTA-Y-879	7.3701	227.42	71 ± 20	3.5	$4.3^{+2.6}_{-1.9}$	...	...
				(32 ± 11)	(3.1)	...	...	...
				(39 ± 10)	(3.9)	...	...	...
REBELS-20	UVISTA-Z-734	7.12†	233.79	<76	...	<4.3	...	...
REBELS-21	UVISTA-Z-013	6.59†	240.75	<53	...	<2.6	<45.0	S22
REBELS-22	UVISTA-Y-657	7.48†	227.42	<46	...	<2.8	...	...
REBELS-23	UVISTA-Z-1410	6.6447	246.96	<78	...	<3.9	...	...
REBELS-24	UVISTA-Y-005	8.35†	202.03	<42	...	<3.2	<38.7	S22
REBELS-25	UVISTA-Y-003	7.3065	227.28	260 ± 22	11.7	$15.4^{+8.4}_{-5.2}$	241.0 ± 30.0	S22
REBELS-26	UVISTA-Z-011	6.5981	246.57	<95	...	<4.7	...	...
REBELS-27	UVISTA-Y-004	7.0898	227.28	51 ± 10	5.1	$2.9^{+1.6}_{-1.1}$	65.0 ± 17.0	S22
REBELS-28	UVISTA-Z-1595	6.9433	244.66	<65	...	<3.5	...	...
REBELS-29	UVISTA-Z-004	6.6847	240.42	56 ± 13	4.4	$2.9^{+1.7}_{-1.1}$	50.0 ± 15.0	B21
REBELS-30	UVISTA-Z-009	6.9823	242.41	<54	...	<3.0	81.7 ± 48.6	B21
REBELS-31	UVISTA-Z-005	6.68†	248.12	<84	...	<4.2	<21.5	B21
REBELS-32	UVISTA-Z-049	6.7290	244.54	60 ± 17	3.5	$3.1^{+1.9}_{-1.3}$	...	...
REBELS-33	UVISTA-Z-018	6.67†	248.12	<80	...	<4.0	...	...
REBELS-34	UVISTA-Z-002	6.6335	248.12	<75	...	<3.8	53.2 ± 32.5	B21
REBELS-35	UVISTA-Z-003	6.97†	239.17	<70	...	<3.8	...	...
REBELS-36	UVISTA-Y-002	7.6772	208.49	<42	...	<2.7	<39.9	S22
REBELS-37	UVISTA-J-1212	7.75†	349.66	97 ± 16	6.1	$5.6^{+1.4}_{-3.1}$	...	...
REBELS-38	UVISTA-Z-349	6.5770	246.57	163 ± 23	7.1	$8.0^{+4.5}_{-2.9}$	...	...
REBELS-39	UVISTA-Z-068	6.8449	244.54	80 ± 16	4.9	$4.2^{+2.4}_{-1.6}$	...	...
REBELS-40	Super8-1	7.3650	223.26	48 ± 13	3.7	$2.9^{+1.7}_{-1.2}$	...	...
REBELS-P1	UVISTA-Z-007	6.7496	245.65	<67	...	<3.4	<52.2	S22
REBELS-P2	UVISTA-Y-008* (Y8)	8.47†	230.36	<65	...	<4.9	<53.7	S22

Table 1 – *continued*

REBELS ID	ALMA source name	Redshift	Observed frequency (GHz)	Continuum flux (μJy)	SNR	L_{IR} (10^{11} L$_\odot$)	F_ν from literature (μJy)	Literature
REBELS-P3	UVISTA-Y-010* (Y10)	7.69[†]	230.36	<66	...	<4.3	<53.6	S22
REBELS-P4	UVISTA-Y-006 (Y6)	8.32[†]	203.08	<53	...	<4.0	<39.6	S22
REBELS-P5	UVISTA-Z-010	7.19[†]	233.99	<59	...	<3.4	<44.1	S22
REBELS-P6	COS-2987030247	6.8075	243.00	<109	...	<5.7	<75.0	S18
REBELS-P7	UVISTA-Z-019	6.7534	245.65	61 ± 16	3.8	$3.2^{+1.9}_{-1.3}$	66.0 ± 23.0	S22
REBELS-P8	COS-3018555981	6.8537	243.00	<122	...	<6.4	65.0 ± 13.0	S22
REBELS-P9	UVISTA-Z-001	7.0599	233.99	55 ± 17	3.3	$3.1^{+1.9}_{-1.4}$	48.1 ± 19.6, 104.0 ± 43.0	B21, S22

correction applied. PYBDSF identifies 'islands' of adjacent emission and then these 'islands' are decomposed by fitting multiple Gaussian functions to find individual sources and their peaks. In this process, PYBDSF uses two signal-to-noise ratios (SNRs) thresholds, iSNR and pSNR, to determine the boundary of an island and the peak of a source, respectively. These thresholds scale with the background rms, which we let the software calculate using the input image. The minimum allowed island size was set to one-third of the number of pixels in the beam area (the default setting of PYBDSF).

The parameters iSNR and pSNR are crucial in ensuring robust detections. In order to test the reliability of detected sources, we used a range of combinations of iSNR and pSNR to perform source extractions on the dust continuum images. The same test was also performed on the reversed science images (hereafter negative images; $-1 \times$ science image). We employed the ranges of $1.0 \leq$ iSNR ≤ 3.0 and $2.0 \leq$ pSNR ≤ 5.0, divided into steps of 0.1 for both of the parameters, but excluded the cases with iSNR > pSNR. For each extraction, we counted the number of detected sources in the science image as a number of positive detections (N_{pos}) and a number of negative detections (N_{neg}) in the reversed image. These numbers were used to evaluate the 'purity' (p) defined as

$$p = \frac{N_{pos} - N_{neg}}{N_{pos}}$$

to indicate the reliability of the detections with a certain set of iSNR and pSNR.

In Fig. 1, we show 2D histograms (colour maps) of p, N_{pos}, and N_{neg} as functions of iSNR and pSNR after combining all of the PYBDSF detections of the entire REBELS sample. Our primary interest is to detect dust emission of the REBELS sources at the phase centre. Thus, we limit the search area for the positive sources in a circular area of 1.5 arcsec radius centred in the pointing field. The detections of negative sources, on the other hand, were performed in the full primary beam area, in order to improve statistics of the detections. Then, N_{neg} was scaled down to match the search area of the positive sources.

The purity increases with both pSNR and iSNR. To maximize the number of reliable detections, we adopted the detection thresholds of (pSNR, iSNR) =(3.3, 2.0), where the purity reaches 95 per cent, for identifying the dust continuum of the REBELS targets. We show N_{pos}, N_{neg}, and p against pSNR (with iSNR = 2.0) in Fig. 2. The purity of the detections in the entire pointing field (including serendipitous detections) is also displayed for comparison. In this case, $p = 95$ per cent is reached at pSNR = 4.2.

In total we detected dust continuum emission with $\geq 3.3\sigma$ in 16 out of the 40 REBELS targets (≥ 40 per cent)[2] in the central $r = 1.5$ arcsec of the images. The detected sources are listed in Table 1 and displayed in Fig. 3 (We show the entire sample including non-detections in Fig. A1.) Among the 16 dust continuum detected sources, three of them do not yet have an emission line detection (REBELS-04, REBELS-06, and REBELS-37). Further ALMA observations for these sources are underway. The dust continuum detections of non-primary target sources will be discussed in a forthcoming paper.

3.2 Dust continuum flux measurements

Based on the dust emission identified with PYBDSF, we measured the dust continuum flux densities at each location of the detections. We employed the IMFIT task in CASA to fit one or more Gaussian components in the dust continuum images. This is because there are some galaxies with complex morphology, for which IMFIT is preferred as an a priori specified number of Gaussians can be fitted.

We limited the fitting region to 3×3 arcsec^2,[3] centred on the source position found by PYBDSF and let IMFIT automatically specify initial parameter estimates of a Gaussian function when there was only a single source. The fitting parameters were peak intensity, peak position, major and minor axis, and position angle. For REBELS-12 and REBELS-19, there are two sources detected by PYBDSF within our detection radius (1.5 arcsec, see Section 3.1). In these cases, we provided initial estimates of the fitting parameters to fit the two sources simultaneously. We have not yet found [C II] emission or a counterpart at shorter wavelengths for either of the secondary sources (the source further from the phase centre with the optical counterpart). It is difficult to assess if these sources are actually at $z \sim 7$ with currently available data sets. In Table 1, we report the fluxes of each of the components and the total fluxes. We investigated the residual image of each source to confirm the fits were adequate.

To determine whether the detected source is resolved or not, we performed Monte Carlo simulations to account for the flux boosting effect due to noise emission (e.g. Algera et al. 2021). In the science images, we inserted in total 20 000 mock point (unresolved) sources[4] and used the same detection method, PYBDSF, to find the sources.

---

[2]This is currently a lower limit because out of the six targets whose observations have not yet been completed, only three at present have a dust continuum detection.

[3]Except for REBELS-40 (Super8-1), where a smaller region (1.5 × 1.8 arcsec^2) was used to avoid a noise peak immediately to the east of the source.

[4]We performed 100 simulations for each science image, with five inserted mock sources in each simulation.
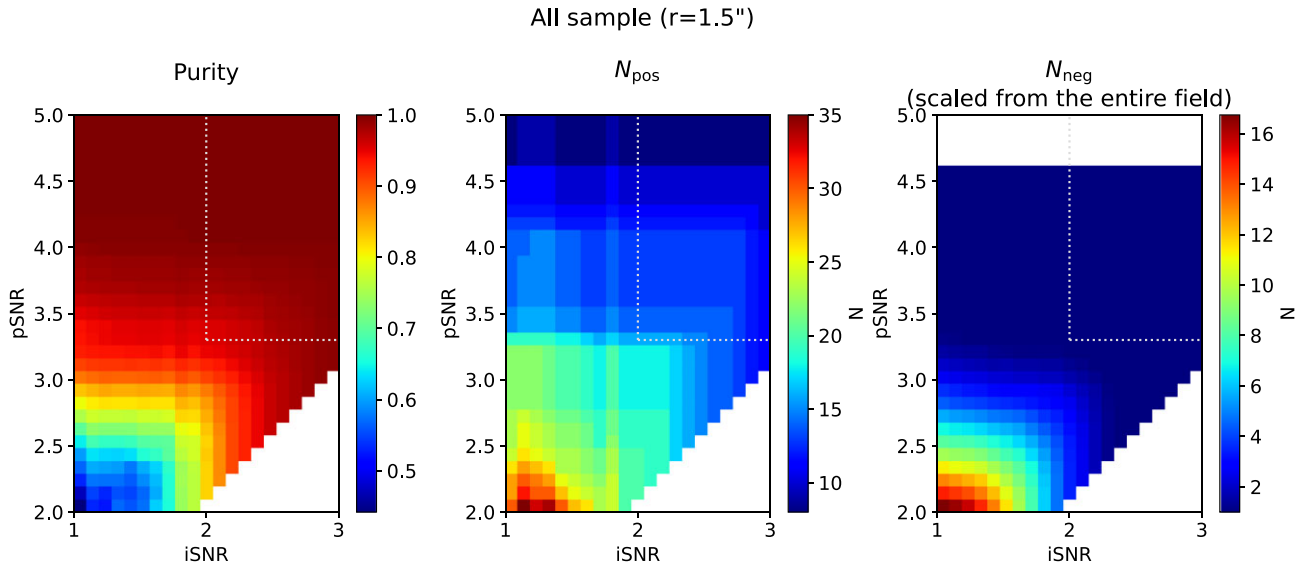
All sample (r=1.5")

Figure 1. From left to right, purity (*p*), the number of detections in the science (positive) image (N_{pos}), and the number of detections in the reversed science (negative) image (N_{neg}). The detections in all of the 40 pointing fields have been combined. The parameters iSNR and pSNR are used in PYBDSF to determine the boundary of an island and the peak of a source, respectively. The detection search for N_{pos} was performed around the phase centre with a 1.5 arcsec radius, while N_{neg} was scaled down to the same area from the detection search of the entire pointing field. The white area in the bottom right of each panel (iSNR > pSNR) was excluded from the analysis. The dotted box indicates the thresholds (pSNR, iSNR) =(3.3, 2.0) for reliable detections ($p \geq 95$ per cent).
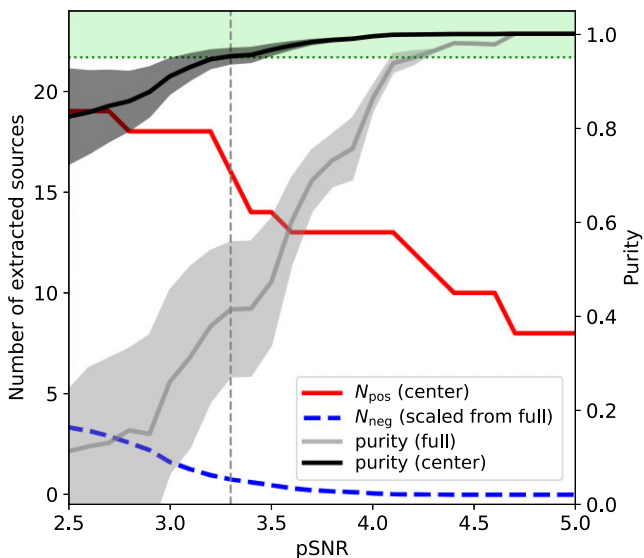
Figure 2. The numbers of positive (N_{pos}; the red solid line) and negative (N_{neg}; the blue dashed line) detections (the left-hand axis) and purity (the right-hand axis) as a function of pSNR when iSNR is fixed at 2.0. The dark and light grey colour lines indicate the purity of the central $r = 1.5$ arcsec and the full pointing field, respectively. The shaded areas represent their standard deviations. At pSNR = 3.3 (the vertical dashed line), purity of ≥ 95 per cent (the light green area) is achieved for the REBELS main targets that are expected to be detected within the central $r = 1.5$ arcsec of the phase centre.

The ratios of recovered integrated and peak flux densities (S_{int} and S_{peak}, respectively) were compared against peak SNR of the sources. The excess from unity in the recovered-to-inserted flux ratio is due to the noise emission boosting the flux. At SNR ~ 8 (SNR ~ 4), the probability that a source is robustly resolved with a 95 per cent confidence level requires a ratio of $S_{int}/S_{peak} > 1.25$ ($S_{int}/S_{peak} \sim 2$), otherwise a ratio above unity is more likely due to underlying

noise. All of the S_{int}/S_{peak} ratios of the REBELS sources indicate that they are unresolved with a 95 per cent probability, except for REBELS-25 that is the brightest source in our sample. Note that both REBELS-12 and REBELS-19 are resolved into two components, but their individual components are not resolved. Thus, in Table 1, the reported flux for REBELS-25 is the IMFIT integrated flux, but the IMFIT peak fluxes for the rest of the sources.

For the REBELS targets without a dust continuum detection, we provide an upper limit in Table 1. To derive the 3σ upper limit, we used the rms noise in each dirty image and scaled it up by a factor of 3. Then we multiplied this by a flux boosting correction factor of 1.33 at SNR = 3 from the same set of simulations described above, based on a comparison of the inserted and recovered peak flux densities. This allows us to avoid underestimating a random noise peak that may appear close to the expected location of a source. This is a reasonable estimate for our targets because it is likely most of the REBELS sources are not resolved in our observations.

Finally, we considered the effect of the cosmic microwave background (CMB) following the prescription of da Cunha et al. (2013). As the CMB temperature increases with redshift, it can affect the dust temperature of high-redshift galaxies with two competing effects: boosting dust continuum emission and reducing background contrast against the dust continuum. We assumed a dust SED with a dust emissivity spectral index (β) of 2.0[5] and a dust temperature (T_d) of 46 K.[6] This is the median T_d of the REBELS sources with both dust and [C II] detections, calculated based on the method proposed by Sommovigo et al. (2021)[7] and adopted to the REBELS

---

[5]We assumed Milky Way-like dust here, which is consistent with recent measurements of high-redshift galaxies (Bowler et al. 2018; da Cunha et al. 2021; Ferrara et al. 2022; Schouws et al. 2022a).
[6]If T_d is 10 K lower (higher), the correction factor would be 6 per cent higher (3 per cent lower).
[7]Although this model assumed a Salpeter IMF (1–100 M$_\odot$) and a metallicity range of 0.3–1 Z$_\odot$, the resulting dust SEDs are not significantly affected.
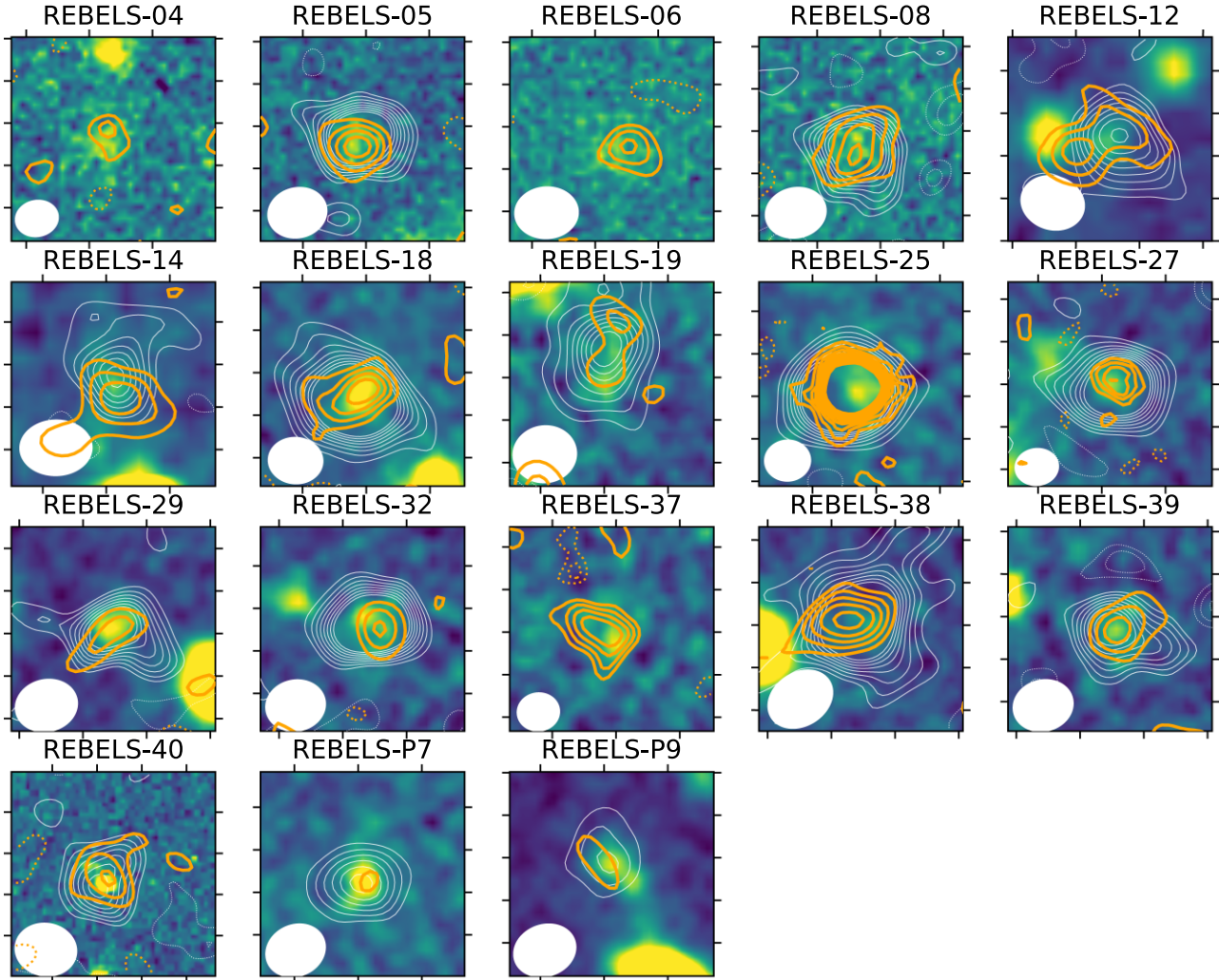
Figure 3. Dust continuum emission (the orange contours) of the REBELS sources. The background images (5×5 arcsec^2) are the stacked *JHK*-band images (or the stacked *JH* images when *K* band is not available). The [C II] emission is also shown by the thin white contours (plotted only when there is a detection with $\geq 3.3\sigma$). The dotted contours indicate negative emission. The contours start from 2σ in steps of 1σ of the background standard deviation. The white ellipses at the bottom left are the beam size.

sources in Sommovigo et al. (2022). The CMB correction factors increase the fluxes in the range of $\sim$4–18 per cent depending on the redshift of each galaxy. Because we currently do not have a robust dust temperature measurement, the continuum flux measurements in Table 1 have not been corrected for the CMB effect. However, the reported L_{IR} were calculated based on the continuum fluxes corrected for the CMB effect.

3.3 Total infrared luminosity

A L_{IR} conversion from a rest-frame 158 μm (or 88 μm) continuum flux was used to acquire L_{IR} (8–1000 μm) or its upper limit for all of the REBELS sources. The conversion factor was computed from the IR SEDs predicted by Sommovigo et al. (2022). This is the same model that was used for deducing T_d above.

This model used the [C II] line luminosity and its underlying dust continuum emission to predict T_d. This model uses the [C II] line luminosity as a proxy for the dust mass, given a [C II]-to-total gas conversion factor derived analytically assuming the Kennicutt–Schmidt relation (Kennicutt 1998) and the $L_{[C II]}$–SFR relation (De

Looze et al. 2014). Then, the underlying continuum emission at 158 μm is used to constrain the T_d and the IR SED of a single temperature modified blackbody. We assumed the same $\beta = 2.0$ as the one used for the CMB correction (see Section 3.2).

For each REBELS source with both [C II] and rest-frame 158 μm continuum detections, L_{IR} was computed using the SED derived with the method above. Based on these L_{IR} and SEDs, a 158 μm-based conversion factor for each galaxy was then calculated. We adopted a single conversion factor for all REBELS sources by taking a median value. This allows us to provide L_{IR} (or its upper limit) for the galaxies without both [C II] and dust continuum emission. The conversion factor is derived in section 3.3.1 in Sommovigo et al. (2022) as

$$L_{IR} = 14 \left(^{+8}_{-5}\right) \nu L_{\nu, 158\,\mu m}.$$

The obtained L_{IR} (or the L_{IR} upper limits) is reported in Table 1.

For a simple comparison, if we instead adopted the SED templates constructed with star-forming galaxies at lower redshifts ($1 \lesssim z \lesssim 3$; e.g. Béthermin et al. 2017; Schreiber et al. 2018), we would obtain a slightly lower conversion factor ($\sim$11) for $L_{\nu, 158\,\mu m}$. Furthermore,

Table 2. Compilation of current dust continuum detections of star-forming galaxies at $z > 6.5$ sorted by redshift. The photometric redshifts are indicated by daggers. The two sources with asterisks are also the REBELS targets, but we do not detect their dust continuum emission (see Section 4).

Source name	Redshift	References
REBELS-04	8.57†	This work
A2744_YD4	8.38	Laporte et al. (2017)
MACS0416_Y1	8.31	Tamura et al. (2019), Bakx et al. (2020)
REBELS-37	7.75†	This work
REBELS-18	7.67	Schouws et al. (2022a), this work
REBELS-19	7.37	This work
REBELS-40	7.36	This work
REBELS-12	7.35	This work
REBELS-25	7.31	Schouws et al. (2022a), Hygate et al. (in preparation), this work
B14-65666	7.15	Bowler et al. (2018), Hashimoto et al. (2019), Sugahara et al. (2021)
A1689-zD1	7.13	Watson et al. (2015), Knudsen et al. (2017), Inoue et al. (2020), Bakx et al. (2021)
REBELS-27	7.09	Schouws et al. (2022a), this work
REBELS-14	7.08	This work
REBELS-P9	7.06	Bowler et al. (2022), Schouws et al. (2022a), this work
ID238225* (REBELS-30)	6.98	Bowler et al. (2022)
REBELS-P8	6.85	Schouws et al. (2022a)
REBELS-39	6.84	This work
REBELS-06	6.80†	This work
REBELS-08	6.75	This work
REBELS-P7	6.75	Schouws et al. (2022a), this work
REBELS-32	6.73	This work
REBELS-29	6.68	Bowler et al. (2022), this work
ID169850* (REBELS-34)	6.63	Bowler et al. (2022)
REBELS-38	6.58	This work
REBELS-05	6.50	This work

if we used a modified blackbody SED with $\beta = 1.6$ and $T_d = 54$ K, which assumed a dust temperature evolution extrapolated to $z = 7$ (Bouwens et al. 2020), then this conversion factor, 11 ± 3, would also be consistent within the uncertainty of the conversion factor used in this work.

There are four REBELS sources for which we targeted [O III] instead of [C II], and thus the rest-frame continuum detection is at rest-frame 88 μm. For these cases, the conversion factor, $L_{IR} = 8(^{+1}_{-4}) \nu L_{\nu, 88\,\mu m}$, was derived from the same SED with the median T_d of the sample that has both the rest-frame 158 μm continuum and [C II] detections. Note that this conversion factor yields about a factor of 3 higher L_{IR} than when a simple modified blackbody (with $T_d = 46$ K and $\beta = 2.0$) is used to fit the single data point at rest-frame 88 μm. This suggests that the dust properties of the [C II]-detected galaxies at $z \sim 7$ and the 88 μm targets at $z \gtrsim 8$ may be different. In fact, the two previously and only known dust continuum detected galaxies at $z > 8$ (Laporte et al. 2017; Bakx et al. 2020, see also Table 2) show different SEDs from the median SED adopted in this work. Both of their dust temperatures are estimated to be higher than $\sim$90 K. If this is also the case for our $z \gtrsim 8$ sample, then these galaxies would have a higher L_{IR} and a lower dust mass than the currently assumed SED that is used to derive the conversion factor.

4 GALAXIES WITH DUST EMISSION AT $z \sim 7$

Although the REBELS data are still not fully acquired, we have detected significant dust continuum emission in 16 REBELS targets

and two from the pilot programs (known as UVISTA-Z-019 and UVISTA-Z-001, respectively, in Schouws et al. 2022a). These two detections are included in the analyses of this paper. There are four galaxies that overlap with Bowler et al. (2022). They reported dust continuum detections in Band 6 for REBELS-29 and REBELS-34, a marginal detection ($\sim$3σ) for REBELS-30, and no detection for REBELS-31, whereas we do not find a detection in REBELS-34 and REBELS-30 with the REBELS data. This is likely due to a shallower depth of the REBELS observations compared to the program of Bowler et al. (2022). Our upper limit estimates are consistent with their flux measurements. In Table 1, we include their flux measurements for completeness. These additional detections lead to a total of 20 dust continuum detections out of the 49 targets of the REBELS and the pilot program ($\geq$40 per cent). This is still a lower limit to what we expect from the full REBELS data set once completed. Among the dust continuum detected galaxies, 15 have been spectroscopically confirmed with the [C II] line at $z > 6.5$.

Together with the pilot observations (Schouws et al. 2022a), REBELS has increased the number of dust continuum detections of star-forming galaxies at $z \sim 7$ by at least a factor of 3 compared with the previously known detections (see Table 2). There are still six sources whose observations have either been partially executed or not yet been executed. Among the targets with partial observations, the dust continuum emission is already detected for REBELS-04, REBELS-06, and REBELS-37, but without any line emission. Based on their photometric redshifts, we are aiming to detect [C II] for REBELS-06 ($z_{photo} = 6.80^{+0.13}_{-0.11}$) and [O III] for REBELS-04 ($z_{photo} = $

8.57$^{+0.10}_{-0.09}$) and REBELS-37 ($z_{\rm photo} = 7.75^{+0.09}_{-0.17}$). The detection rate of at least 40 per cent in the REBELS sample suggests that it is not uncommon for galaxies at $z \sim 7$ to have significant dust continuum emission and host obscured star formation.

In the following subsections, we discuss the rest-frame UV and IR properties of the dust continuum detected galaxies in the REBELS sample. We adopted a prescription of $\rm SFR_{UV} = 7.1 \times 10^{-29} L_\nu$ [$\rm M_\odot\, yr^{-1}$ (erg s^{-1} Hz^{-1})$^{-1}$] and $\rm SFR_{IR} = 1.2 \times 10^{-10} L_{IR}$ [$\rm M_\odot\, yr^{-1}\, L_\odot^{-1}$] (the same as Bouwens et al. 2022). The derived SFRs are summarized in Table 3.

4.1 Physical properties of the dust-detected galaxies at $z \sim 7$

Armed with our large sample of $z > 6.5$ galaxies with multiple rest-UV and optical detections, we show the physical properties of the galaxies with and without dust continuum detections in Fig. 4.

The number fractions of the dust continuum detected sources are ~ 0.4 across the $M_{\rm UV}$ range with a hint of an increasing trend towards the less UV luminous end. Although uncertainties are large, the UV continuum slope ($\beta_{\rm UV}$, defined as $L_\lambda \propto \lambda_{\rm UV}^\beta$) of the dust-detected sources tends to be redder (larger $\beta_{\rm UV}$) relative to the non-detections. Almost all of the observed sources that are detected with dust continuum have $\beta_{\rm UV} > -1.8$, but there are two exceptions, REBELS-10 and REBELS-13. They have a red UV slope ($\beta_{\rm UV} > -1.5$) but no dust detection. Neither of them have a [C II] detection. Additional analyses reveal that these two sources may well be lower redshift interlopers. Newly available deeper *Spitzer*/InfraRed Array Camera (IRAC) observations (Stefanon & Bouwens 2019), which became available after the targeting of REBELS-10, put the photometric redshift of this source at $z < 6$. For REBELS-13, the integrated redshift likelihood distribution at $z < 6$ is >15 per cent. Detailed discussions on each of these sources will be presented in Stefanon et al. (in preparation). More detailed analyses of $\beta_{\rm UV}$ and dust properties (e.g. the IRX–$\beta_{\rm UV}$ relation) will be presented in Bowler et al. (in preparation).

On the other hand, we do not see a clear trend in the dust extinction in the V band (A_V) and stellar mass (M_*) from the SED fitting. The limited rest-frame optical/NIR coverage we have of targets results in large uncertainties on estimates of the stellar mass (see also Topping et al. 2022). None of these relations are statistically significant (p-value >0.05) with the two-sample Kolmogorov–Smirnov test to reject the null hypothesis that the distributions of the dust continuum detected and undetected samples are identical. Future observations with the *James Webb Space Telescope* (*JWST*) are essential for better constraints on these fundamental properties of $z \sim 7$ galaxies (cf. the Cycle-1 General Observer Program ID 1626, PI: Stefanon).

4.2 Infrared properties of the dust-detected galaxies at $z \sim 7$

All of the dust continuum detected galaxies have $L_{\rm IR} \gtrsim 3 \times 10^{11}\, \rm L_\odot$ and the detections are present up to $z \sim 8.5$ (Fig. 5). They are in the class of luminous infrared galaxies (LIRGs) with $10^{11} < L_{\rm IR}/\rm L_\odot < 10^{12}$, except for REBELS-25 that is instead classified as an ultraluminous infrared galaxy (ULIRG, $10^{12} < L_{\rm IR}/\rm L_\odot < 10^{13}$; Hygate et al., in preparation). According to the model of Zavala et al. (2021), the obscured star formation is dominated (~ 80 per cent) by galaxies with $L_{\rm IR} > 10^{12}\, \rm L_\odot$ at $z \sim 7$. Therefore, we might have expected to detect more galaxies with $L_{\rm IR} > 10^{12}\, \rm L_\odot$ in the REBELS sample. This discrepancy could be due to the REBELS target selection being based on rest-UV luminosity, which may miss most obscured populations, as opposed to a blind survey. In addition,

Table 3. SFRs derived based on UV and IR, and the total (UV + IR) for the REBELS sample.

| REBELS ID	SFR$_{\rm UV}$ ($\rm M_\odot\, yr^{-1}$)	SFR$_{\rm IR}$ ($\rm M_\odot\, yr^{-1}$)	SFR$_{\rm UV + IR}$ ($\rm M_\odot\, yr^{-1}$)
REBELS-01	43$^{+5}_{-4}$	<34	<78
REBELS-02	22$^{+4}_{-4}$	<29	<51
REBELS-03	16$^{+4}_{-4}$	<33	<50
REBELS-04	26$^{+1}_{-1}$	54$^{+19}_{-32}$	80$^{+19}_{-32}$
REBELS-05	13$^{+3}_{-2}$	39$^{+22}_{-15}$	52$^{+22}_{-15}$
REBELS-06	15$^{+4}_{-3}$	48$^{+28}_{-18}$	63$^{+28}_{-19}$
REBELS-07	21$^{+6}_{-5}$	<33	<54
REBELS-08	16$^{+7}_{-5}$	63$^{+36}_{-24}$	79$^{+37}_{-25}$
REBELS-09	50$^{+16}_{-12}$	<41	<91
REBELS-10	37$^{+12}_{-9}$	<41	<78
REBELS-11	39$^{+9}_{-7}$	<69	<109
REBELS-12	30$^{+10}_{-7}$	62$^{+38}_{-27}$	92$^{+39}_{-28}$
REBELS-13	44$^{+10}_{-8}$	<65	<109
REBELS-14	36$^{+16}_{-11}$	40$^{+24}_{-17}$	76$^{+28}_{-20}$
REBELS-15	33$^{+11}_{-8}$	<43	<76
REBELS-16	30$^{+2}_{-2}$	<44	<74
REBELS-17	14$^{+3}_{-3}$	<47	<61
REBELS-18	27$^{+4}_{-3}$	42$^{+24}_{-16}$	69$^{+24}_{-16}$
REBELS-19	14$^{+3}_{-3}$	51$^{+31}_{-22}$	65$^{+31}_{-23}$
REBELS-20	17$^{+2}_{-2}$	<52	<68
REBELS-21	18$^{+4}_{-3}$	<32	<50
REBELS-22	25$^{+3}_{-2}$	<34	<58
REBELS-23	14$^{+9}_{-5}$	<47	<61
REBELS-24	20$^{+5}_{-4}$	<39	<59
REBELS-25	14$^{+3}_{-3}$	185$^{+101}_{-63}$	199$^{+101}_{-63}$
REBELS-26	17$^{+2}_{-2}$	<56	<73
REBELS-27	18$^{+4}_{-4}$	34$^{+20}_{-13}$	52$^{+20}_{-14}$
REBELS-28	30$^{+9}_{-7}$	<42	<72
REBELS-29	24$^{+3}_{-3}$	34$^{+20}_{-14}$	59$^{+20}_{-14}$
REBELS-30	27$^{+2}_{-2}$	<35	<62
REBELS-31	26$^{+4}_{-2}$	<51	<76
REBELS-32	14$^{+2}_{-2}$	37$^{+23}_{-16}$	51$^{+23}_{-16}$
REBELS-33	13$^{+2}_{-2}$	<48	<61
REBELS-34	30$^{+2}_{-2}$	<45	<75
REBELS-35	31$^{+3}_{-3}$	<46	<77
REBELS-36	23$^{+5}_{-4}$	<33	<56
REBELS-37	24$^{+1}_{-1}$	67$^{+16}_{-37}$	91$^{+16}_{-37}$
REBELS-38	17$^{+4}_{-4}$	96$^{+54}_{-35}$	114$^{+54}_{-35}$
REBELS-39	38$^{+6}_{-5}$	50$^{+29}_{-20}$	88$^{+30}_{-20}$
REBELS-40	17$^{+1}_{-1}$	35$^{+21}_{-15}$	52$^{+21}_{-15}$
REBELS-P1	25$^{+3}_{-2}$	<41	<66
REBELS-P2	15$^{+6}_{-4}$	<59	<74
REBELS-P3	14$^{+5}_{-4}$	<51	<65
REBELS-P4	18$^{+9}_{-6}$	<48	<66
REBELS-P5	25$^{+3}_{-3}$	<41	<65
REBELS-P6	16$^{+2}_{-2}$	<68	<84
REBELS-P7	14$^{+2}_{-2}$	38$^{+23}_{-16}$	52$^{+23}_{-16}$
REBELS-P8	17$^{+2}_{-1}$	<77	<94
REBELS-P9	49$^{+3}_{-3}$	37$^{+23}_{-16}$	86$^{+23}_{-17}$
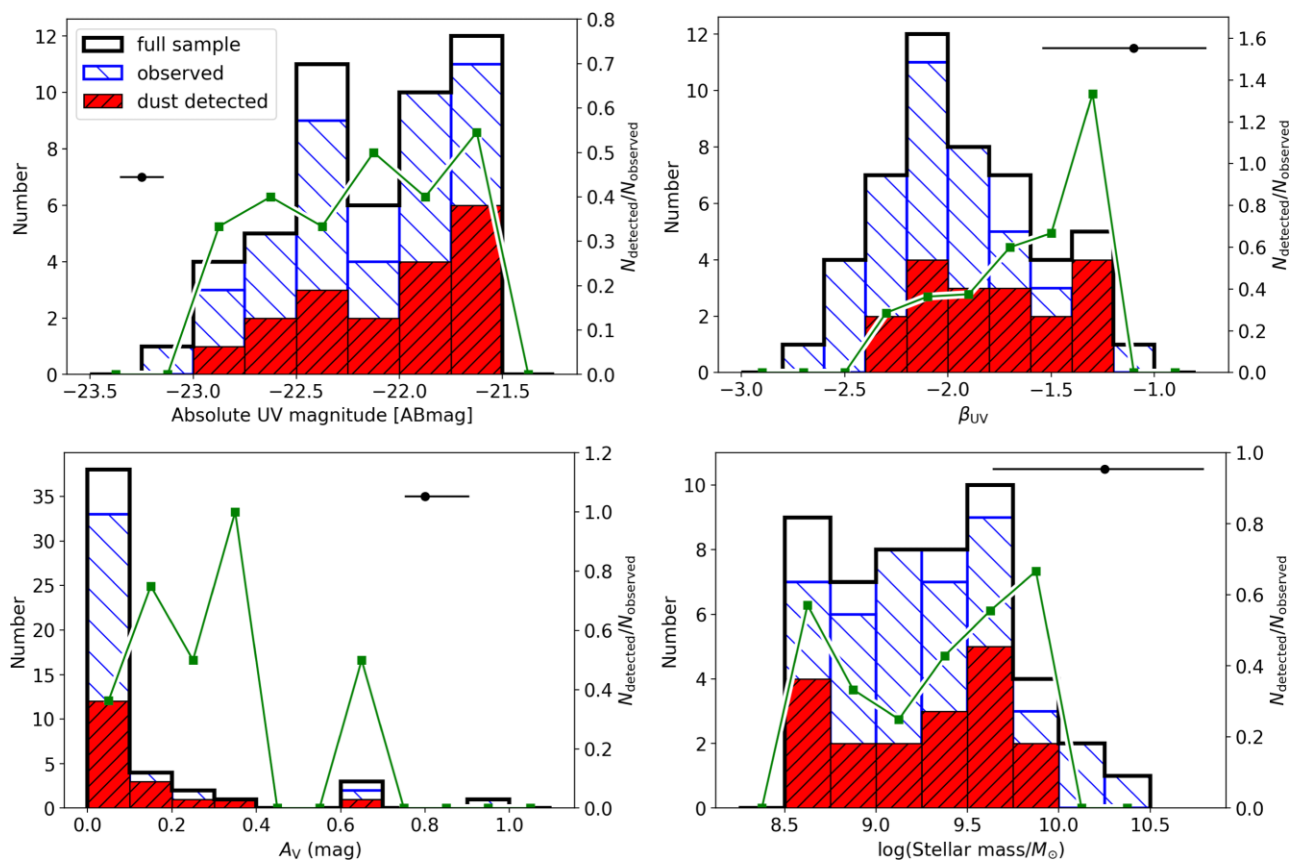
Figure 4. The physical properties ($M_{\rm UV}$, $\beta_{\rm UV}$, A_V, and M_*) as derived from SED fitting to the rest-UV photometry of the REBELS sources. The typical error of the measured parameters is shown by a black dot and a horizontal line in each panel. The numbers of the REBELS sources with and without dust continuum detections are shown in the red and blue histograms, respectively. The black empty histogram denotes the entire REBELS sample, including the targets whose observations have not yet been completed. The green line indicates the number fraction (the right-hand axis) of the dust continuum detected sources (red) against the fully observed sources (red).

the discrepancy could arise from the assumed faint-end slope of the IR luminosity function in the model of Zavala et al. (2021). They adopted the faint-end slope from the luminosity functions at $1 \lesssim z \lesssim 3$ derived by the ALMA SPECtroscopic Survey in the UDF (ASPECS) program at 1 and 3 mm (González-López et al. 2019, 2020; Aravena et al. 2020). The 2 mm survey performed by Zavala et al. (2021) (and Casey et al. 2021) covers a wider but shallower area, and thus provides a robust constraint for more luminous sources. If there is an evolution in the faint-end slope to become steeper towards the distant universe, then galaxies with lower IR luminosities would contribute more to the obscured star formation at $z \sim 7$. A IR luminosity function based on the REBELS sources will be shown in Barrufet et al. (in preparation) and the obscured star formation density at $z \sim 7$ will be presented in Algera et al. (in preparation).

Despite the UV selection of the REBELS targets, the fraction of dust obscured star formation, $\mathrm{SFR}_{\rm IR}/\mathrm{SFR}_{\rm UV+IR}$, is high in the dust continuum detected galaxies. As shown in Fig. 6, with the REBELS detection limit, any galaxy with a dust continuum detection is $\gtrsim 50$ per cent obscured. The obscured fraction ranges from ≈ 50 per cent to ≈ 90 per cent (Bowler et al. 2022; Schouws et al. 2022a). This is in agreement with the obscuration of ~ 50–90 per cent (except one source with 28 per cent but agrees within the errors) with an independent method in the REBELS sources found by Ferrara et al. (2022) (see also Dayal et al. 2022). Schneider et al. (in preparation) have also investigated this wide spread of the
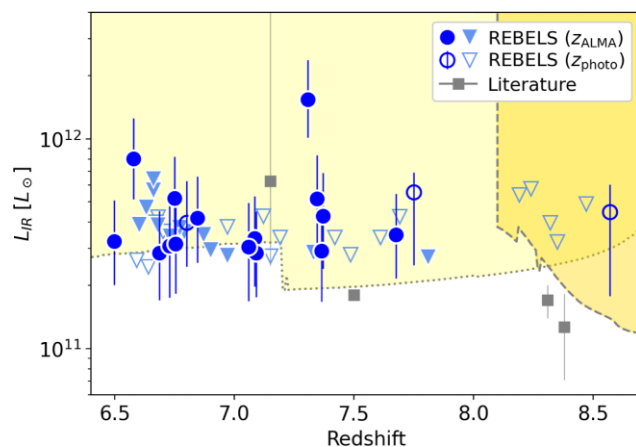
Figure 5. $L_{\rm IR}$ versus redshift for the REBELS sources and the earlier results from literature (Table 2). The dust continuum detected sources are displayed as the blue circles. The light blue triangles are upper limits of the dust non-detected sources. For the sources with a [C II] detection, their spectroscopic redshifts are used (the filled symbols), otherwise a photometric redshift is adopted (the open symbols). The 3σ detection limits of the REBELS observations for the continuum emission for the [C II] and [O III] scans are shown in the background as the light yellow region with the dotted line and the dark yellow region with the dashed line, respectively.
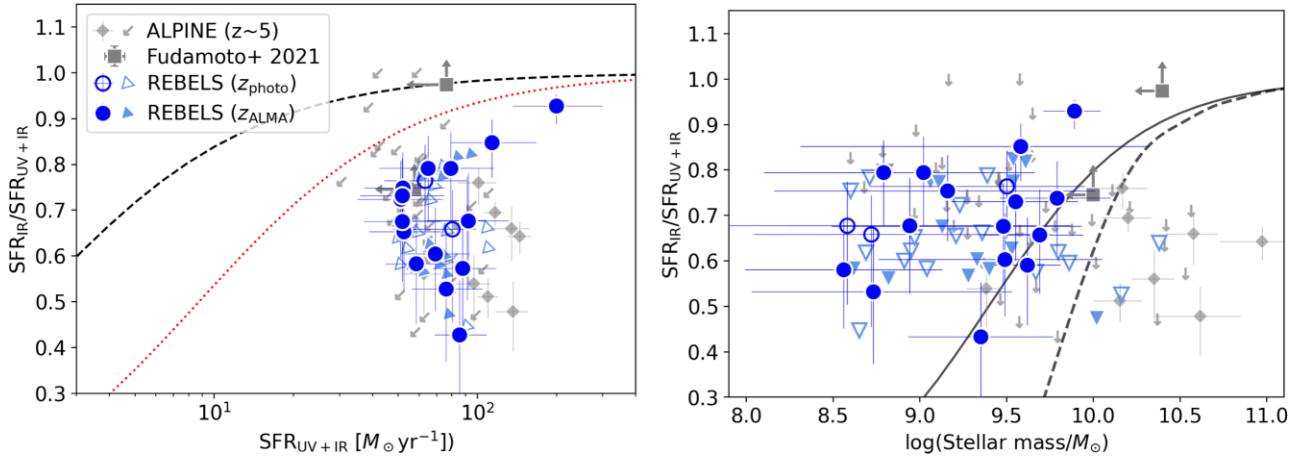
Figure 6. Fraction of obscured star formation rate (SFR_{IR}/SFR_{UV+IR}) as a function of total SFR (left) and stellar mass (right). The symbols are the same as in Fig. 5. The limits of the two serendipitously detected $z \sim 7$ galaxies are shown by the filled grey squares (Fudamoto et al. 2021). The $z \sim 5$ ALPINE sources (Fudamoto et al. 2020) are shown by diamonds for the continuum detected and by arrows as the upper limits for the non-detected sources. In the left-hand panel, the black dashed and red dotted lines indicate the relation at $0.5 < z < 1.0$ and $2.0 < z < 2.5$, respectively (Whitaker et al. 2017, with the Dale & Helou 2002 SED templates). In the right-hand panel, the black solid line and dashed line represent the relations with the SED templates of Dale & Helou (2002) and Kirkpatrick et al. (2015)/Magdis et al. (2012), respectively, at $0.5 < z < 2.5$ where no evolution is seen (Whitaker et al. 2017).

obscuration fraction with simulations in detail. The obscured fraction of our $z \sim 7$ galaxies is in a similar range to the ALPINE galaxies at $z \sim 5$ with direct dust continuum detections (Fudamoto et al. 2020).

As shown in the left-hand panel of Fig. 6, the obscured fraction of our $z \sim 7$ galaxies are on average lower for a given SFR, compared to the trend of a stellar mass-completed galaxy sample at $z \lesssim 2.5$ (Whitaker et al. 2017, with the Dale & Helou 2002 SED templates). The slope of the obscured fraction evolves from $z \sim 2.5$ to $z \sim 0$ (e.g. Reddy et al. 2006, 2008; Whitaker et al. 2017). Although the lower obscured fraction of the REBELS galaxies could be due to the sample selection of UV bright galaxies (yet the obscured fraction is $\approx$50–90 per cent), this may suggest that the evolution continues from $z \sim 7$.

On the contrary, the relation between obscured fraction and stellar mass does not evolve in the range $0 \lesssim z \lesssim 2.5$ (the right-hand panel of Fig. 6; see also fig. 6 in Dayal et al. 2022). Given that the stellar mass measurements of the REBELS galaxies are still uncertain (and could be underestimated in the cases of constant SFH assumptions; Topping et al. 2022), the REBELS galaxies may be in general consistent with the relation found at low redshift. There are a couple of outliers, such as REBELS-25 (the brightest continuum detection) and serendipitously detected sources without a detection in the rest-UV (Fudamoto et al. 2021), that lie above the $SFR_{IR}/SFR_{UV+IR}-M_*$ relation. Excluding these extreme sources, the dependence of the obscured fraction on stellar mass at $0 \lesssim z \lesssim 2.5$ and $z \sim 7$ may not evolve significantly. Interestingly, however, the ALPINE dust detected galaxies at $z \sim 5.5$, mostly lie below the relation at $0 \lesssim z \lesssim 2.5$ (Fudamoto et al. 2020). In the stellar mass range of 10^9–10^{10} $M_\odot$, where 2/3 of the REBELS dust-detected galaxies are, the stack of the ALPINE galaxies does not detect any dust continuum emission. This could be due to the difference in the sample selection between ALPINE and REBELS,[8] but may also imply a wide variety of fractions of obscured star formation at $z > 2.5$. More discussions on the obscured fraction at $z \sim 7$, including a stacking analysis, will be presented in Algera et al. (in preparation). Better constraints

on L_{IR} with ALMA and stellar mass with *JWST* are imperative to further investigate overall dust obscuration and its relationship to stellar mass and SFR of $z \sim 7$ galaxies.

5 DUST MORPHOLOGY AND SPATIAL OFFSET BETWEEN UV AND IR

We discern a small number of galaxies resolved in rest-frame UV imaging, while the majority of the dust emission is marginally resolved or unresolved in our data with the spatial resolution of $\sim$1.2–1.6 arcsec. In addition, we see physical displacements between rest-UV and far-IR emission in a handful of the REBELS dust continuum detected galaxies.

5.1 Dust morphology

It is notable that two of the dust continuum detected targets, REBELS-12 and REBELS-19, consist of two dust emission components. In both cases, the component closer to where the UV emission is located (the primary component, hereafter) is fainter than the other component. Both of the galaxy systems also have a [C II] detection, but neither of them shows double peaks similar to the dust emission. With the current data, it is difficult to assess whether both of the dust components originate from the target galaxy or whether one of them is from another unknown galaxy.

For REBELS-12, there is another rest-UV emitting source shown in the *JHK*-stacked image with a 0.8 arcsec separation from the secondary dust component (the dust emission component that is offset from the UV location of the target source). Interestingly, in the same field of view (FoV; primary beam) of the REBELS-12 observation, there is a serendipitous detection of a galaxy at the same redshift confirmed by [C II][9] with dust continuum emission (Fudamoto et al. 2021). It is not clear with the current data if the offset dust component of REBELS-12 is related to this overdensity.

---

[8] The ALPINE targets were selected based on UV spectroscopy and cover a lower stellar mass range than the REBELS sample.

[9] The REBELS main target is at $z = 7.347$ and the serendipitous galaxy is at $z = 7.352$ with a $\sim$11.5 arcsec spatial separation.

In the case of REBELS-19, there is no obvious object in the *JHK*-stacked image that may be associated with the secondary dust component. Its [C II] emission also shows an offset from the UV emission, but peaking between the two dust components. The morphology of the UV emission seems to be elongated in the north–south direction, along the dust emission. Deeper observations and a higher spatial resolution in both dust continuum and UV are necessary to further investigate their physical structures.

Among galaxies with a single dust component, there is one object, REBELS-25, that appears to be clearly resolved in both rest-UV and IR (see Section 3.2). This object has the highest L_{IR} in the REBELS sample with $1.5^{+0.8}_{-0.5} \times 10^{12}$ L$_\odot$. Its high SNR detection allows us to infer that this source is resolved at a <1 arcsec scale. The deconvolved size reported by IMFIT is $(0.74 \pm 0.17 \text{ arcsec}) \times (0.69 \pm 0.22 \text{ arcsec})$, corresponding to $(3.75 \pm 0.89) \text{ kpc} \times (3.53 \pm 1.10) \text{ kpc}$. This source also shows a spatial offset towards the west in-between the clumpy UV emission (Stefanon et al. 2019; Schouws et al. 2022a). For a more detailed study on REBELS-25, we refer to Hygate et al. (in preparation).

Although our Monte Carlo simulations (Section 3.2) do not indicate that the other sources are resolved, there are some sources that potentially show elongated emission. In fact, an observation with deeper and higher spatial resolution conducted by Bowler et al. (2022) has identified an extended tail in REBELS-29. In the REBELS data, we also discern this tail but with less significance.

For the rest of the unresolved REBELS galaxies, unfortunately the limited spatial resolution makes it hard to discuss their morphology in further detail. The spatial resolution of ~1.2 arcsec of our observations corresponds to a physical size of ~6.3 kpc at $z = 7$. This is at the high end of the dust size measured at $z \sim 0–2$ (Cheng et al. 2020; Tadaki et al. 2020). Higher spatial resolution observations are needed to investigate whether a more compact dust extent compared with stellar emission is also seen at $z \sim 7$ to explore mechanisms of stellar mass growth in the first billion years of the Universe (e.g. Hodge & da Cunha 2020; Inoue et al. 2020; Ivison et al. 2020; Herrera-Camus et al. 2021; Popping et al. 2022).

5.2 Spatial offset between rest-UV and IR

Spatial offsets in the peak emission between the rest-frame UV and far-IR have become evident in galaxies at $z > 6.5$ and at lower redshifts with recent high spatial resolution observations at submillimetre and millimetre wavelengths (see e.g. Hodge et al. 2012, 2016; Carniani et al. 2017; Laporte et al. 2017; Rujopakarn et al. 2019 for observational, and e.g. Behrens et al. 2018; Liang et al. 2019; Sommovigo et al. 2020; Cochrane et al. 2021 for theoretical studies). The spatial displacement between the rest-UV and far-IR could depend on the process of how dust and stars have been assembled (e.g. Cochrane et al. 2019; Zanella et al. 2021; Ferrara et al. 2022), but also bias analyses that are based on the UV–IR energy balance (e.g. IRX-β, SED fitting; Barisic et al. 2017; Bowler et al. 2022). Here, we explore the prevalence of a spatial offset between the rest-UV and dust emission in UV-selected galaxies at $z \sim 7$ from REBELS and how it relates to the galaxy properties.

We determine the peaks of the rest-UV and dust continuum emission by a 2D Gaussian fit to avoid being biased to a clump or accidentally picking up a noise peak. We let the amplitude, *xy* positions, and rotation be free parameters for the fit, whereas the *xy* width and background level are fixed to 1 pixel and zero, respectively. We show the determined peak locations of the rest-UV and dust emission in Fig. 7.

Based on the defined peak locations, we then calculate the spatial offsets between the rest-UV and dust emission. The measured offsets are listed in Table 4. The two galaxies, REBELS-12 and REBELS-19, with the double dust emission peaks show the largest offsets among the sample, 0.7 arcsec (3.5 kpc) and 1.5 arcsec (7.6 kpc), respectively (see also Section 5.1 for their morphologies). REBELS-38 also has a prominent offset of 0.6 arcsec (3.3 kpc). The spatial offset of REBELS-25 has been reported in Schouws et al. (2022a) and is discussed in more detail in Hygate et al. (in preparation).

To explore whether the UV–IR spatial segregation affects other observed physical properties of the galaxies, we compare the UV-dust offset to galaxy properties in Fig. 8. The top three panels show comparisons of L_{IR}, IRX, and β_{UV} against the UV–IR separation, but no significant trend has been found. If a correlation with IRX or the UV slope exists, galaxies being outliers in the IRX-β_{UV} relation could be due to a larger spatial separation between the rest-UV and dust emission peaks. This may be related to the recent findings of Bowler et al. (2022), who presented the IRX-β_{UV} relation of five galaxies at $z \sim 7$ with UV-dust spatial offsets. All of these galaxies (one is reported in this work as well) have $\beta_{UV} \lesssim -2.0$. It is possible that galaxies with spatially decoupled UV and IR emission tend to show an unusually blue colour in the UV (see also theoretical work by Behrens et al. 2018; Sommovigo et al. 2020). However, a larger sample of galaxies with a moderate to large spatial offset observed with higher spatial resolution imaging is needed to confirm whether β_{UV} and centroid locations of the UV and dust are physically related.

Motivated to search for this decoupled UV and IR emission, we also compare the spatial offsets with I_m, the molecular index, defined as

$$I_m = \frac{F_{158}/F_{1500}}{\beta_{UV} - \beta_{UV, int}},$$

where F_{158} and F_{1500} are the observed continuum flux densities at rest-frame 158 μm and 1500 Å, respectively, and $\beta_{UV, int}$ is the intrinsic UV slope from a model (see Ferrara et al. 2022 for more details, as well as Pallottini et al. 2017; Behrens et al. 2018). A high value of I_m implies a large IR-to-UV flux ratio (i.e. red colour) compared to the galaxy UV spectral slope. Such values can only be obtained if the galaxy has a multiphase ISM made of star forming, opaque clumps, and a diffuse component that is relatively transparent to UV light emitted by young stars (see Ferrara et al. 2022 for a more detailed discussion). No statistically significant correlation is seen between I_m and the UV–IR separation, given the Spearman rank correlation coefficient is 0.65 with a *p*-value of 0.44. Although we cannot exclude the null hypothesis of no correlation, increasing I_m with the UV–IR offset, in a simple picture, indicates that star formation in these early galaxies has a (possibly slightly older) star formation site where the dust has already been cleared up, accompanied by another younger star formation site still embedded in dusty molecular clouds.

There are indeed some galaxies in the epoch of reionization that have been speculated to contain two stellar populations to elucidate their observed features. Although it is not detected with dust emission, the red rest-frame optical colour of a gravitationally lensed star-forming galaxy MACS1149-JD1 at $z = 9.1$ indicates that it already experienced a star-forming phase at $z \approx 15$ (Hashimoto et al. 2018, also see the discussion in Roberts-Borsani, Ellis & Laporte 2020). Another example is GN-z11, which first was discovered via a spectroscopically identified rest-UV continuum break at $z = 11$ (Oesch et al. 2016). Recently, this galaxy has been confirmed by Jiang et al. (2021) at this redshift with the [C III] λ1907, C III] λ1909
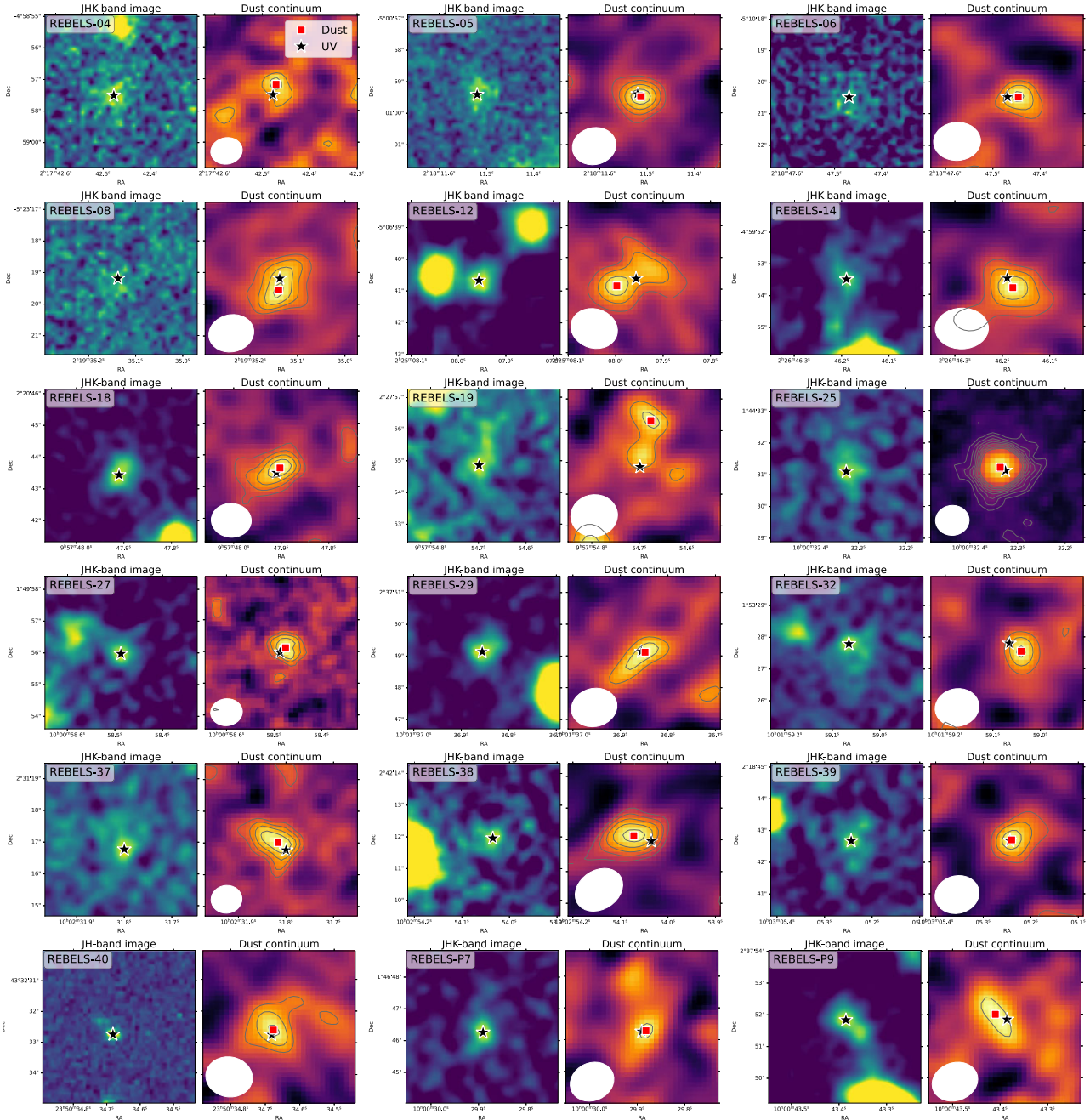
Figure 7. Peak locations of rest-UV (on the left of each panel) and dust (on the right of each panel) emission of the REBELS dust continuum detected sources. The peaks of the UV and dust emission are indicated as the black star and red square, respectively. The rest-UV image shown here is a stack of *JHK*-band images (or *JH* when *K* is not available).

doublet, and O III] λ1666. Assuming no contribution from an active galactic nucleus (AGN), its observed high rest-frame equivalent width (>20 Å) of C III] indicates the presence of a young stellar population. Its moderate stellar mass, $(1.3 \pm 0.6) \times 10^9 \, M_\odot$, also requires a relatively evolved population to be present. Additionally, the two $z \sim 13$ candidates of star-forming galaxies reported by Harikane et al. (2022) may also support an onset of star formation at $z > 10$. Mancini et al. (2016) found that in order to simultaneously reproduce the observed UV luminosity function and the relation between β_{UV} and UV magnitude in their model, they have to assume a

two-phase distribution for dust, with two different dust optical depths. However, alternatively, it is also possible that a large I_m is caused by a merging system of an obscured galaxy and an optically thin galaxy (cf. REBELS-25; Hygate et al., in preparation). Although we cannot draw firm conclusions regarding the mass and dust assembly of these very early galaxies with the limited resolution of the current data, our systematic observations of dusty galaxies at $z \sim 7$ provide important clues of the build-up of stellar mass and dust in galaxies in the early universe (see also Dayal et al. 2022; Pallottini et al. 2022; Tacchella et al. 2022).

Table 4. Measured offset between the UV and dust peak emission, listed together with β_{UV} (Bouwens et al. 2022) and I_m (Ferrara et al. 2022). For REBELS-04, REBELS-06, and REBELS-37, due to a lack of a spectroscopic redshift, as indicated by daggers, their photometric redshifts are used instead to calculate I_m.

REBELS ID	Δ(UV-dust) (arcsec)	β_{UV}	I_m
REBELS-04	0.34 ± 0.06	$-2.15^{+0.20}_{-0.38}$	$^\dagger 423^{+172}_{-95}$
REBELS-05	0.13 ± 0.04	$-1.29^{+0.36}_{-0.44}$	191^{+75}_{-84}
REBELS-06	0.34 ± 0.05	$-1.24^{+0.67}_{-0.35}$	$^\dagger 200^{+122}_{-80}$
REBELS-08	0.37 ± 0.07	$-2.17^{+0.58}_{-0.58}$	1183^{+457}_{-457}
REBELS-12	0.65 ± 0.25	$-1.99^{+0.48}_{-0.76}$	384^{+161}_{-197}
REBELS-14	0.35 ± 0.57	$-2.21^{+0.41}_{-0.47}$	435^{+159}_{-166}
REBELS-18	0.19 ± 0.05	$-1.34^{+0.19}_{-0.32}$	111^{+34}_{-40}
REBELS-19	1.50 ± 0.06	$-2.33^{+0.45}_{-0.64}$	3870^{+1544}_{-1719}
REBELS-25	0.19 ± 0.03	$-1.85^{+0.56}_{-0.46}$	1772^{+660}_{-585}
REBELS-27	0.23 ± 0.04	$-1.79^{+0.42}_{-0.45}$	229^{+84}_{-86}
REBELS-29	0.12 ± 0.14	$-1.61^{+0.10}_{-0.19}$	129^{+40}_{-42}
REBELS-32	0.44 ± 0.07	$-1.50^{+0.28}_{-0.30}$	213^{+84}_{-85}
REBELS-37	0.34 ± 0.04	$-1.24^{+0.16}_{-0.27}$	$^\dagger 261^{+89}_{-133}$
REBELS-38	0.57 ± 0.25	$-2.18^{+0.45}_{-0.42}$	1786^{+571}_{-555}
REBELS-39	0.06 ± 0.08	$-1.96^{+0.30}_{-0.28}$	224^{+72}_{-71}
REBELS-40	0.16 ± 0.03	$-1.44^{+0.29}_{-0.36}$	165^{+64}_{-69}
REBELS-P7	0.13 ± 0.04	$-2.09^{+0.14}_{-0.15}$	639^{+215}_{-217}
REBELS-P9	0.40 ± 0.12	$-1.76^{+0.17}_{-0.33}$	87^{+33}_{-36}

6 CONCLUSIONS

In this paper, we presented the dust continuum source identifications and flux extractions of the UV-selected galaxies at $z > 6.5$ of the ALMA Large Program REBELS and its pilot programs. The main results are summarized as follows.

(i) Out of the 40 REBELS targets, we detected 16 galaxies that have rest-frame ~88 or 158 μm dust continuum emission with $\geq 3.3\sigma$ where the purity is 95 per cent. There are still six targets whose observations remain to be completed, making the current detection rate ≥ 40 per cent. Together with the REBELS pilot programs, which adds an additional nine galaxies, we obtained 18 dust continuum detections at $z > 6.5$ out of a total of 49 targets. This, in turn, increases the sample of dusty star-forming galaxies in the epoch of reionization by a factor of more than 3.

(ii) The spatial resolution of the observations ranged between 1.2 and 1.6 arcsec. Based on Monte Carlo simulations, to identify resolved dust emission, we found that one galaxy (REBELS-25) shows a spatially resolved structure. In addition, two galaxies (REBELS-12 and REBELS-19) show double components in their dust continuum emission.

(iii) IR luminosities of the dust continuum detected galaxies are in a range of $3 \times 10^{11} \lesssim L_{IR}/L_\odot \lesssim 2 \times 10^{12}$ with one galaxy classified as a ULIRG. Despite being UV-selected targets, the dust continuum detected galaxies have a high fraction of obscured star formation (~50–90 per cent).

(iv) We also found that some of the dust continuum detected galaxies exhibit spatially decoupled rest-UV and far-IR emission. However, with current limited spatial resolution imaging, no clear trend has been seen in L_{IR}, IRX, β_{UV}, and I_m against the
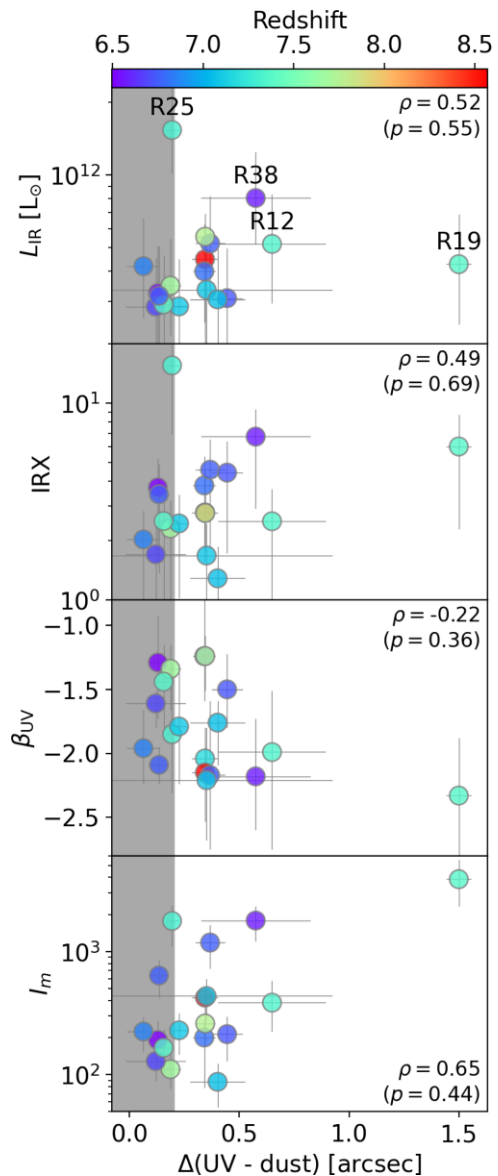
Figure 8. Galaxy physical properties against spatial offsets. From the top to bottom, IR luminosity (L_{IR}), UV spectral slope (β_{UV}), infrared excess (IRX), and molecular index (I_m). The symbols are colour coded by their spectroscopic redshifts where available, and the others are photometric redshifts. The grey region indicates the separation below the expected astrometric uncertainty of the ALMA observations (see Section 2.1). The Spearman rank correlation coefficient (ρ) and the associated p-value are shown in each panel.

UV–IR separation. To confirm the speculated two different populations in single galaxies (or a merging system) during the epoch of reionization, higher spatial resolution observations are needed.

The REBELS program has provided a first statistical glimpse of obscured star formation in UV-selected galaxies at $z > 6.5$. In the near future, multiband ALMA coverage will help to better constrain dust SEDs and improve measurements on dust temperature and mass. Together with resolved studies of individual sources, this will facilitate our understanding of star formation and dust build-up in the first billion years of the Universe.

ACKNOWLEDGEMENTS

DATA AVAILABILITY

Table 1 in this paper is available at the Centre de Données astronomiques de Strasbourg (CDS), at https://xxx. The other data generated in this research will be shared on reasonable request to the corresponding author.

REFERENCES

Algera H. S. B. et al., 2021, ApJ, 912, 73
Aoyama S., Hou K.-C., Shimizu I., Hirashita H., Todoroki K., Choi J.-H., Nagamine K., 2017, MNRAS, 466, 105
Aoyama S., Hou K.-C., Hirashita H., Nagamine K., Shimizu I., 2018, MNRAS, 478, 4905
Aravena M. et al., 2020, ApJ, 901, 79
Bakx T. J. L. C. et al., 2020, MNRAS, 493, 4294
Bakx T. J. L. C. et al., 2021, MNRAS, 508, L58
Barisic I. et al., 2017, ApJ, 845, 41
Behrens C., Pallottini A., Ferrara A., Gallerani S., Vallini L., 2018, MNRAS, 477, 552
Béthermin M. et al., 2017, A&A, 607, A89
Bouwens R. J. et al., 2016, ApJ, 833, 72
Bouwens R. et al., 2020, ApJ, 902, 112
Bouwens R. J. et al., 2022, ApJ, 931, 160
Bowler R. A. A., Bourne N., Dunlop J. S., McLure R. J., McLeod D. J., 2018, MNRAS, 481, 1631
Bowler R. A. A., Cullen F., McLure R. J., Dunlop J. S., Avison A., 2022, MNRAS, 510, 5088
Bruzual G., Charlot S., 2003, MNRAS, 344, 1000
Calzetti D., Armus L., Bohlin R. C., Kinney A. L., Koornneef J., Storchi-Bergmann T., 2000, ApJ, 533, 682
Capak P. L. et al., 2015, Nature, 522, 455
Carniani S. et al., 2017, A&A, 605, A42
Casey C. M. et al., 2021, ApJ, 923, 215
Chabrier G., 2003, PASP, 115, 763
Cheng C. et al., 2020, MNRAS, 499, 5241
Chevallard J., Charlot S., 2016, MNRAS, 462, 1415
Cochrane R. K. et al., 2019, MNRAS, 488, 1779
Cochrane R. K. et al., 2021, MNRAS, 503, 2622
da Cunha E. et al., 2013, ApJ, 766, 13
da Cunha E. et al., 2021, ApJ, 919, 30
Dale D. A., Helou G., 2002, ApJ, 576, 159
Dayal P. et al., 2022, MNRAS, 512, 989
De Barros S., Oesch P. A., Labbé I., Stefanon M., González V., Smit R., Bouwens R. J., Illingworth G. D., 2019, MNRAS, 489, 2355
De Looze I. et al., 2014, A&A, 568, A62
Dunlop J. S. et al., 2017, MNRAS, 466, 861
Ferland G. J. et al., 2013, Rev. Mex. Astron. Astrofis., 49, 137
Ferrara A. et al., 2022, MNRAS, 512, 58
Franco M. et al., 2020a, A&A, 643, A30
Franco M. et al., 2020b, A&A, 643, A53
Fudamoto Y. et al., 2020, A&A, 643, A4
Fudamoto Y. et al., 2021, Nature, 597, 489
Gaia Collaboration et al., 2016, A&A, 595, A1
Gaia Collaboration et al., 2021, A&A, 649, A1
Ginolfi M., Graziani L., Schneider R., Marassi S., Valiante R., Dell'Agli F., Ventura P., Hunt L. K., 2018, MNRAS, 473, 4538
González-López J. et al., 2019, ApJ, 882, 139
González-López J. et al., 2020, ApJ, 897, 91
Graziani L., Schneider R., Ginolfi M., Hunt L. K., Maio U., Glatzle M., Ciardi B., 2020, MNRAS, 494, 1071
Grogin N. A. et al., 2011, ApJS, 197, 35

Gruppioni C. et al., 2013, MNRAS, 432, 23
Gruppioni C. et al., 2020, A&A, 643, A8
Gutkin J., Charlot S., Bruzual G., 2016, MNRAS, 462, 1757
Harikane Y. et al., 2022, ApJ, 929, 1
Hashimoto T. et al., 2018, Nature, 557, 392
Hashimoto T. et al., 2019, PASJ, 71, 71
Herrera-Camus R. et al., 2021, A&A, 649, A31
Hodge J. A., da Cunha E., 2020, R. Soc. Open Sci., 7, 200556
Hodge J. A., Carilli C. L., Walter F., de Blok W. J. G., Riechers D., Daddi E., Lentati L., 2012, ApJ, 760, 11
Hodge J. A. et al., 2016, ApJ, 833, 103
Howell J. H. et al., 2010, ApJ, 715, 572
Inoue A. K., Hashimoto T., Chihara H., Koike C., 2020, MNRAS, 495, 1577
Ivison R. J., Richard J., Biggs A. D., Zwaan M. A., Falgarone E., Arumugam V., van der Werf P. P., Rujopakarn W., 2020, MNRAS, 495, L1
Jarvis M. J. et al., 2013, MNRAS, 428, 1281
Jiang L. et al., 2021, Nat. Astron., 5, 256
Kennicutt R. C., Jr, 1998, ApJ, 498, 541
Khusanova Y. et al., 2021, A&A, 649, A152
Kirkpatrick A., Pope A., Sajina A., Roebuck E., Yan L., Armus L., Díaz-Santos T., Stierwalt S., 2015, ApJ, 814, 9
Knudsen K. K., Watson D., Frayer D., Christensen L., Gallazzi A., Michałowski M. J., Richard J., Zavala J., 2017, MNRAS, 466, 138
Koprowski M. P. et al., 2016, ApJ, 828, L21
Koprowski M. P. et al., 2018, MNRAS, 479, 4355
Laporte N. et al., 2017, ApJ, 837, L21
Laporte N. et al., 2021, MNRAS, 505, 4838
Lawrence A. et al., 2007, MNRAS, 379, 1599
Leśniewska A., Michałowski M. J., 2019, A&A, 624, L13
Liang L. et al., 2019, MNRAS, 489, 1397
Ma X. et al., 2019, MNRAS, 487, 1844
McCracken H. J. et al., 2012, A&A, 544, A156
McLure R. J. et al., 2018, MNRAS, 476, 3991
McMullin J. P., Waters B., Schiebel D., Young W., Golap K., 2007, in Shaw R. A., Hill F., Bell D. J., eds, ASP Conf. Ser. Vol. 376, Astronomical Data Analysis Software and Systems XVI. Astron. Soc. Pac., San Francisco, p. 127
Madau P., Dickinson M., 2014, ARA&A, 52, 415
Magdis G. E. et al., 2012, ApJ, 760, 6
Magnelli B. et al., 2013, A&A, 553, A132
Mancini M., Schneider R., Graziani L., Valiante R., Dayal P., Maio U., Ciardi B., Hunt L. K., 2015, MNRAS, 451, L70
Mancini M., Schneider R., Graziani L., Valiante R., Dayal P., Maio U., Ciardi B., 2016, MNRAS, 462, 3130
Mohan N., Rafferty D., 2015, Astrophysics Source Code Library, record ascl:1502.007
Nath B. B., Sethi S. K., Shchekinov Y., 1999, MNRAS, 303, 1
Novak M. et al., 2017, A&A, 602, A5
Oesch P. A. et al., 2016, ApJ, 819, 129
Oke J. B., Gunn J. E., 1983, ApJ, 266, 713
Pallottini A., Ferrara A., Bovino S., Vallini L., Gallerani S., Maiolino R., Salvadori S., 2017, MNRAS, 471, 4128
Pallottini A. et al., 2022, MNRAS, 513, 5621

Popping G., Puglisi A., Norman C. A., 2017, MNRAS, 472, 2315
Popping G. et al., 2022, MNRAS, 510, 3321
Postman M. et al., 2012, ApJS, 199, 25
Reddy N. A., Steidel C. C., Fadda D., Yan L., Pettini M., Shapley A. E., Erb D. K., Adelberger K. L., 2006, ApJ, 644, 792
Reddy N. A., Steidel C. C., Pettini M., Adelberger K. L., Shapley A. E., Erb D. K., Dickinson M., 2008, ApJS, 175, 48
Roberts-Borsani G. W., Ellis R. S., Laporte N., 2020, MNRAS, 497, 3440
Rujopakarn W. et al., 2019, ApJ, 882, 107
Schouws S. et al., 2022a, ApJ, 928, 31
Schouws S. et al., 2022b, preprint (arXiv:2202.04080)
Schreiber C., Elbaz D., Pannella M., Ciesla L., Wang T., Franco M., 2018, A&A, 609, A30
Scoville N. et al., 2007, ApJS, 172, 38
Smit R. et al., 2018, Nature, 553, 178
Smolčić V. et al., 2017, A&A, 602, A1
Sommovigo L., Ferrara A., Pallottini A., Carniani S., Gallerani S., Decataldo D., 2020, MNRAS, 497, 956
Sommovigo L., Ferrara A., Carniani S., Zanella A., Pallottini A., Gallerani S., Vallini L., 2021, MNRAS, 503, 4878
Sommovigo L. et al., 2022, MNRAS, 513, 3122
Sparke L. S., Gallagher J. S., III, 2000, Galaxies in the Universe: An Introduction. Cambridge Univ. Press, Cambridge
Stark D. P. et al., 2017, MNRAS, 464, 469
Stefanon M., Bouwens R., 2019, Spitzer Proposal ID #14305
Stefanon M. et al., 2019, ApJ, 883, 99
Sugahara Y. et al., 2021, ApJ, 923, 5
Tacchella S. et al., 2022, ApJ, 927, 170
Tadaki K.-i. et al., 2020, ApJ, 901, 74
Tamura Y. et al., 2019, ApJ, 874, 27
Topping M. W. et al., 2022, preprint (arXiv:2203.07392)
Trenti M. et al., 2011, ApJ, 727, L39
Wakelam V. et al., 2017, Mol. Astrophys., 9, 1
Watson D., Christensen L., Knudsen K. K., Richard J., Gallazzi A., Michałowski M. J., 2015, Nature, 519, 327
Whitaker K. E., Pope A., Cybulski R., Casey C. M., Popping G., Yun M. S., 2017, ApJ, 850, 208
Yamaguchi Y. et al., 2019, ApJ, 878, 73
Yamaguchi Y. et al., 2020, PASJ, 72, 69
Yan H. et al., 2011, ApJ, 728, L22
Zanella A., Pallottini A., Ferrara A., Gallerani S., Carniani S., Kohandel M., Behrens C., 2021, MNRAS, 500, 118
Zavala J. A. et al., 2021, ApJ, 909, 165

APPENDIX A: NIR IMAGES AND DUST CONTINUUM CONTOURS OF THE ENTIRE SAMPLE

In Fig. A1, we show the stacked *JHK*-band images (or *JH*-band images when *K*-band image is not available) with the contours of dust continuum emission for all of the REBELS sample.
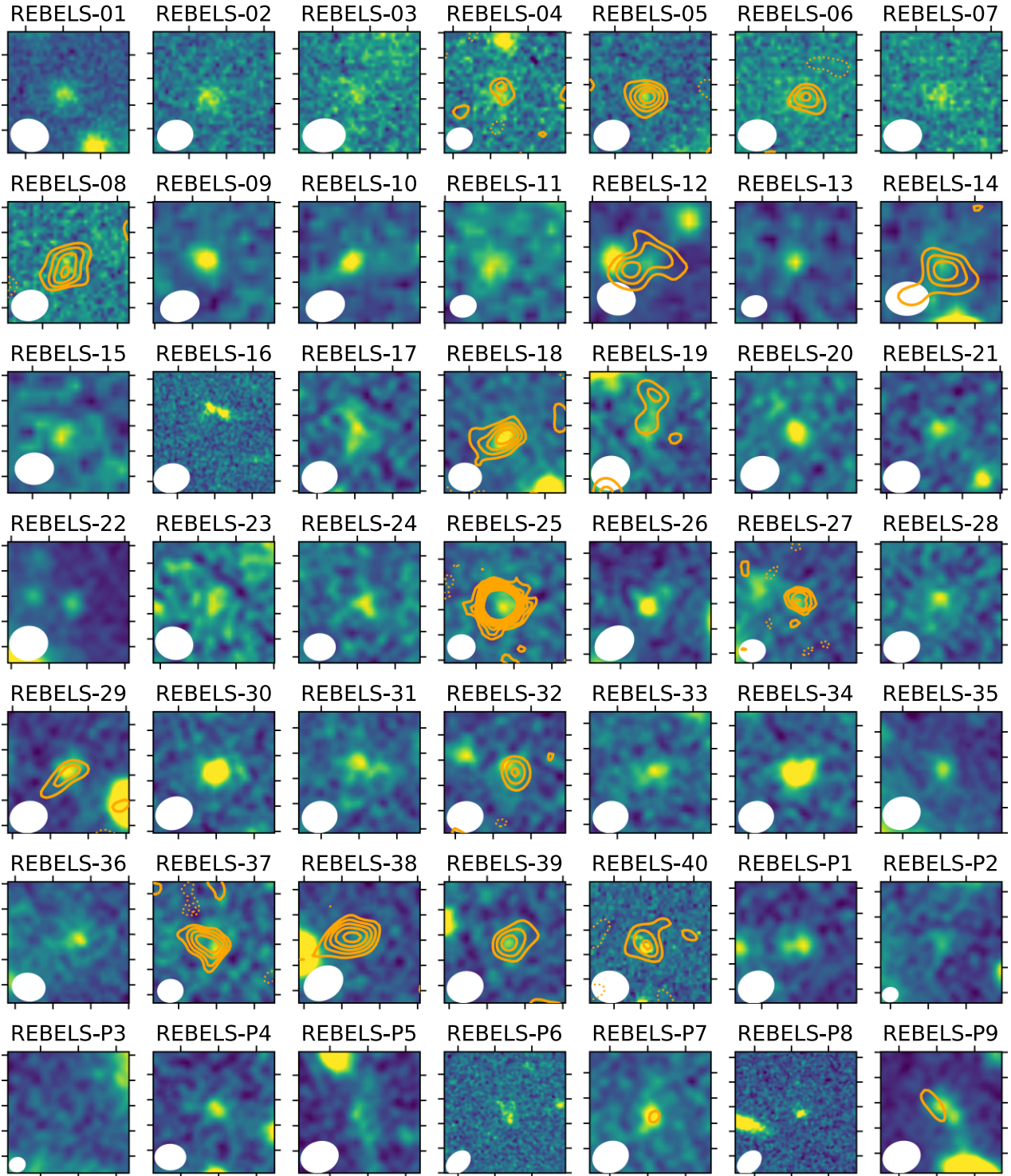
Figure A1. The same as Fig. 3 without the [C II] contours. The targets without a dust continuum detection are also shown.

[1] *Hiroshima Astrophysical Science Center, Hiroshima University, 1-3-1 Kagamiyama, Higashi-Hiroshima, Hiroshima 739-8526, Japan*
[2] *National Astronomical Observatory of Japan, 2-21-1 Osawa, Mitaka, Tokyo 181-8588, Japan*
[3] *Leiden Observatory, Leiden University, NL-2300 RA Leiden, the Netherlands*
[4] *Scuola Normale Superiore, Piazza dei Cavalieri 7, I-56126 Pisa, Italy*
[5] *Astrophysics Research Institute, Liverpool John Moores University, 146 Brownlow Hill, Liverpool L3 5RF, UK*

[6] *Jodrell Bank Centre for Astrophysics, Department of Physics and Astronomy, School of Natural Sciences, The University of Manchester, Manchester M13 9PL, UK*
[7] *Steward Observatory, University of Arizona, 933 N Cherry Ave, Tucson, AZ 85721, USA*
[8] *Observatoire de Genéve, CH-1290 Versoix, Switzerland*
[9] *Cosmic Dawn Center (DAWN), Niels Bohr Institute, University of Copenhagen, Jagtvej 128, DK-2200 København N, Denmark*

[10]*Nucleo de Astronomia, Facultad de Ingenieria y Ciencias, Universidad Diego Portales, Av. Ejercito 441, Santiago, Chile*

[11]*International Centre for Radio Astronomy Research, University of Western Australia, 35 Stirling Hwy, Crawley 26, WA 6009, Australia*

[12]*Kapteyn Astronomical Institute, University of Groningen, PO Box 800, NL-9700 AV Groningen, the Netherlands*

[13]*Sterrenkundig Observatorium, Ghent University, Krijgslaan 281 – S9, B-9000 Gent, Belgium*

[14]*Department of Physics and Astronomy, University College London, Gower Street, London WC1E 6BT, UK*

[15]*Research Institute for Science and Engineering, Waseda University, 3-4-1 Okubo, Shinjuku, Tokyo 169-8555, Japan*

[16]*Departmento de Astronomia, Universidad de Chile, Casilla 36-D, Santiago 7591245, Chile*

[17]*Centro de Astrofisica y Tecnologias Afines (CATA), Camino del Observatorio 1515, Las Condes, Santiago 7591245, Chile*

[18]*Dipartimento di Fisica, Sapienza, Universita di Roma, Piazzale Aldo Moro 5, I-00185 Roma, Italy*

[19]*INAF/Osservatorio Astrofisico di Arcetri, Largo E. Femi 5, I-50125 Firenze, Italy*

[20]*Centre for Astrophysics and Supercomputing, Swinburne University of Technology, PO Box 218, Hawthorn, VIC 3112, Australia*

[21]*I. Physikalisches Institut, Universität zu Köln, Zülpicher Strasse 77, D-50937 Köln, Germany*

[22]*INAF/Osservatorio Astronomico di Roma, Via Frascati 33, I-00078 Monte Porzio Catone, Roma, Italy*

This paper has been typeset from a TeX/LaTeX file prepared by the author.